

TR/02/90

March 1990

Development Progress of
Program FESTER
X. D. Pan and M. B. Reed

**Technical Report on Development Progress
of Program FESTER**

by

X. D. Pan and M. B. Reed

March, 1990

Department of Maths, and Stats.,
Brunel University,
Uxbridge UB8 3PH, U.K.

BRUNEL UNIVERSITY
SEP 1991
LIBRARY

w919536x

ction

ary of history

STER can do

Developments

ge description

ssor:

:

Ults

ptions of some few features

eformation analysis

metric analysis

method of simulating excavation

cation examples

problem in a deep level coal mine

ge tunnel near a reservoir

ng tunnel face

nces

1. Introduction

1.1 A summary of history

The computer program **FESTER** (Finite Element Simulation of Tunnel Excavated in Rocks) was originally developed on an SERC/British Coal co-funded research project at the Oxford University Computing Laboratory between 1985 and 1986. Since the end of 1986, it has been continuously developed at the Department of Mathematics and Statistics of Brunei University under the support of SERC (current grant is to finish in 1992) and British Coal (finished in 1988). The program structure is based on the linear elastic finite element package FINEPACK developed at the Department of Civil Engineering of University College of Swansea (Naylor 1977, Hinton & Owen 1977). FESTER is developed to model the deformation and stresses in the rock mass surrounding underground openings and predict the failure behaviour of rock masses. It uses elasto-viscoplastic theory for the nonlinear analysis. The detailed theory and features including a user's guide can be found in a previous report (Reed and Lavender 1989). Some of the work involved in the development of the program were also reported in several published papers by the main developer (Reed 1986a, 1986b, 1988a, 1988b). Since 1989, the program has been further developed to incorporate a few other features based on the co-operative research work at the Rock Mechanics Research Group of Imperial College (Pan 1988, Pan and Hudson 1988, Pan et al 1989).

1.2 What FESTER can do

Program FESTER is an elasto-viscoplastic 2-D (or axisymmetric) finite element model for analysis of rock and rock masses behaviour. The features

and the analysis it can provide are as follows:

Element types:

FESTER is focused on the use of

- a. the isoparametric 8-noded quadrilateral element for representing the rock masses,
- b. the 5-noded mapped infinite element for representing far field boundary, and
- c. the 6-noded joint element for discontinuities.

Nonlinear techniques:

Incremental (tangent stiffness) approach with implicit ($0 < \theta \leq 1$) or explicit ($\theta = 0$) time integration algorithm. Use of non-symmetric frontal solver. Options for large deformation analysis with Updated Lagrangian formulation.

Rock mass models:

Orthotropic elasticity; elastic joint interface; brittle/strain softening failure or yield with Mohr-Coulomb, Drucker-Prager or Hoek-Brown 3-D surface; nonassociated flow rule with Drucker-Prager or the extended Hoek-Brown flow function. Options for other two failure modes: tensile crack and fracture along bedding planes.

Types of loading:

Point loads; distributed edge loads, body forces; gravity and other in situ stress field; incremental loading; two ways of simulating excavation (opposite

nodal forces or reduction of stress and stiffness).

Boundary conditions:

Infinite elements to model far field boundary condition; prescribed values of displacement or pressure at the boundary element sides.

1.3 Further development

The package is currently under development to extend the 2-D version straightforwardly to a 3-D version. This requires more sophisticated 3-D graphical input and output techniques for communication with the main analysis. The project is expected to finish in 1992.

2 Package description

Full details of the FESTER package and the underlying theory are available in Reed & Lavender (1988). Only brief summary will be given here.

2.1 Preprocessor

The separate preprocessor suite of programs runs on an IBM PC (or compatible machine), and includes graphical programs using Halo graphics software. It enables interactive preparation of data files for large problems, using mesh refinement. The user inputs nodal co-ordinates, boundary conditions, etc. for a coarse mesh containing just sufficient 'macro elements' to define the basic geometry of the problem. Loading is also applied to the coarse mesh (point loads may be added after refinement). Mesh refinement is performed by simply specifying the subdivision required along an edge of a macro-element. The preprocessor automatically carries this refinement through the mesh of macro-elements, and moreover it automatically assigns the appropriate boundary conditions, material properties and loading to the elements of the refined mesh.

Once the refinement is complete, the elements must be re-numbered so that the solution of the global stiffness equation in the main program – performed by the frontal method - will be performed efficiently; that is, the frontwidth of the assembled system must be reduced. This frontwidth reduction is performed by the preprocessor without further user input.

Figure 2.1 shows the options available when the preprocessor is run.

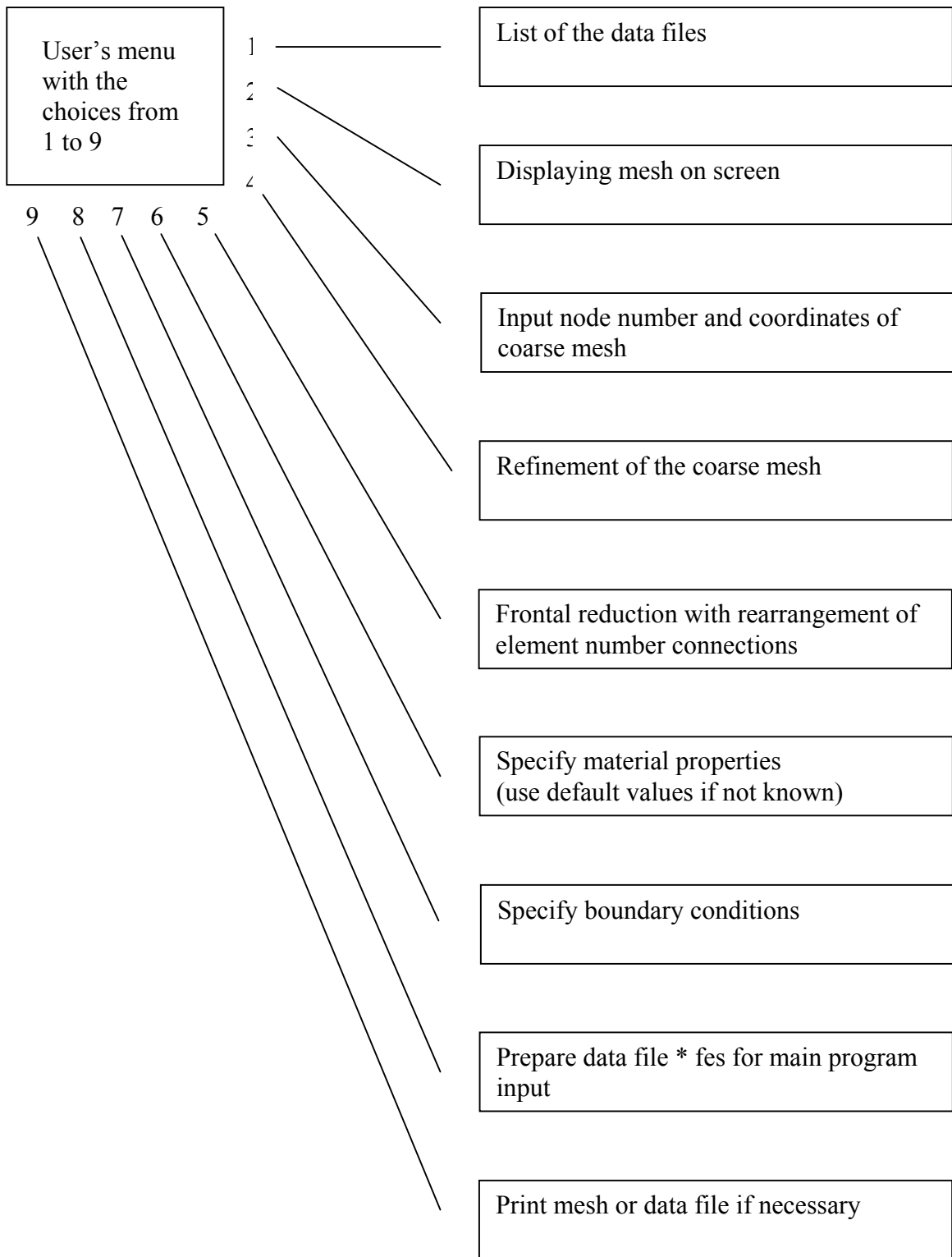


Figure 2.1 Preprocessor window options.

2.2 Analysis

An outline of the main **FESTER** program has been given above, with each element is associated one of the following material models:

- 1 Linear elastic structure (no in situ stress in gravity loading).
- 2 Isotropic linear elastic rocks.
- 3 Orthotropic linear elastic rocks.
- 4 Isotropic elastic-plastic rocks with Mohr-Coulomb failure surface.
- 5 Isotropic elastic-plastic rocks with Hoek-Brown failure surface.
- 6 Orthotropic elastic-plastic rocks with Mohr-Coulomb failure surface.
- 7 Orthotropic elastic-plastic rocks with Hoek-Brown failure surface.
- 8 Isotropic elastic-plastic rocks with Drucker-Prager failure surface.
- 9 Elastic joint interface in rocks.

The material property parameters required with these models are listed below:

Component No.	Symbol	Description	Used in mat, models
1	E	Young's Modulus	1; 2; 4; 5; 8; 9
	E_1	Orthotropic Young's Modulus	3; 6; 7
	k_1	Normal joint stiffness	9
2	ν	Poisson's ratio	1; 2; 4; 5; 8; 9
	ν_1	Orthotropic Poisson's ratio	3; 6; 7;
	k_2	Tangential joint stiffness	9
3	E_2	Orthotropic Young's modulus	3; 6; 7
4	ν_2	Orthotropic Poisson's ratio	3; 6; 7
5	G	Orthotropic shear modulus	3; 6; 7
6	B	Angle of cross orthotropy	3; 6; 7
7	σ_c	Intact rock strength	4; 5; 6; 7; 8
8	k	Initial triaxial stress factor	4; 6; 8
	m	Hoek-Brown empirical parameter	5; 7
9	S	Initial strength parameter	4; 5; 6; 7; 8
10	α	Dilation parameter	4; 5; 6; 7; 8
11	kI	Residual triaxial stress factor	4; 6; 8
	mI	Residual Hoek-Brown parameter	5; 7
12	s^I	Residual strength parameter	4; 5; 6; 7; 8
13	γ	Fluidity parameter	4; 5; 6; 7; 8
14	ϕ_j	Frictional angle of 'beddings'	6; 7
15	c_j	Cohesion of 'beddings'	6; 7
16	ψ_j	Dilation parameter of 'beddings'	6; 7
17	γ_j	Fluidity parameter of 'beddings'	6; 7
18	σ_{ten}	Tensile strength	4; 5; 6; 7; 8
19	σ^I_{ten}	Residual tensile strength	4; 5; 6; 7; 8

Table 2.1 Material property parameters used in FESTER.

A novel feature of the elasto-viscoplastic models in finite element analyses is the distinction between an initial yield surface (at which plastic behaviour first occurs) and a residual surface to which the stress state moves after yield. A low-tension criterion - again with initial and residual tensile strengths - is also available, and with orthotropic materials a plane-of-weakness ('beddings') may also be defined; no tension is allowed normal to this plane, and a Coulomb friction law operates parallel to the plane. The flow rules for the various criteria are combined as in the multilaminate model (Zinkiewicz and Pande 1977).

There are thus three independent modes in which plastic deformation may arise: through the yield criterion of the rock mass (Mohr-Coulomb or Hoek-Brown), by tensile cracking, and by sliding/cracking along a plane of weakness for orthotropic materials.

The main analysis produces output giving the stress state at each sampling point and displacement at each node, for each time step; this may be restricted, to save paper, to stress points where yield has occurred, and nodes on the excavation boundary, at the start and end of each load increment. The full output data is also available in a file for input to the post-processor for graphical display. The system is summarised in Figure 2.2.

2.3 Post-processor

Graphical output for selected portions of the mesh may be obtained, showing principal stresses and displacements; examples are given in the results below. It is possible to distinguish the failure modes which have become active at each stress point. The system is summarised in Figure 2.3.

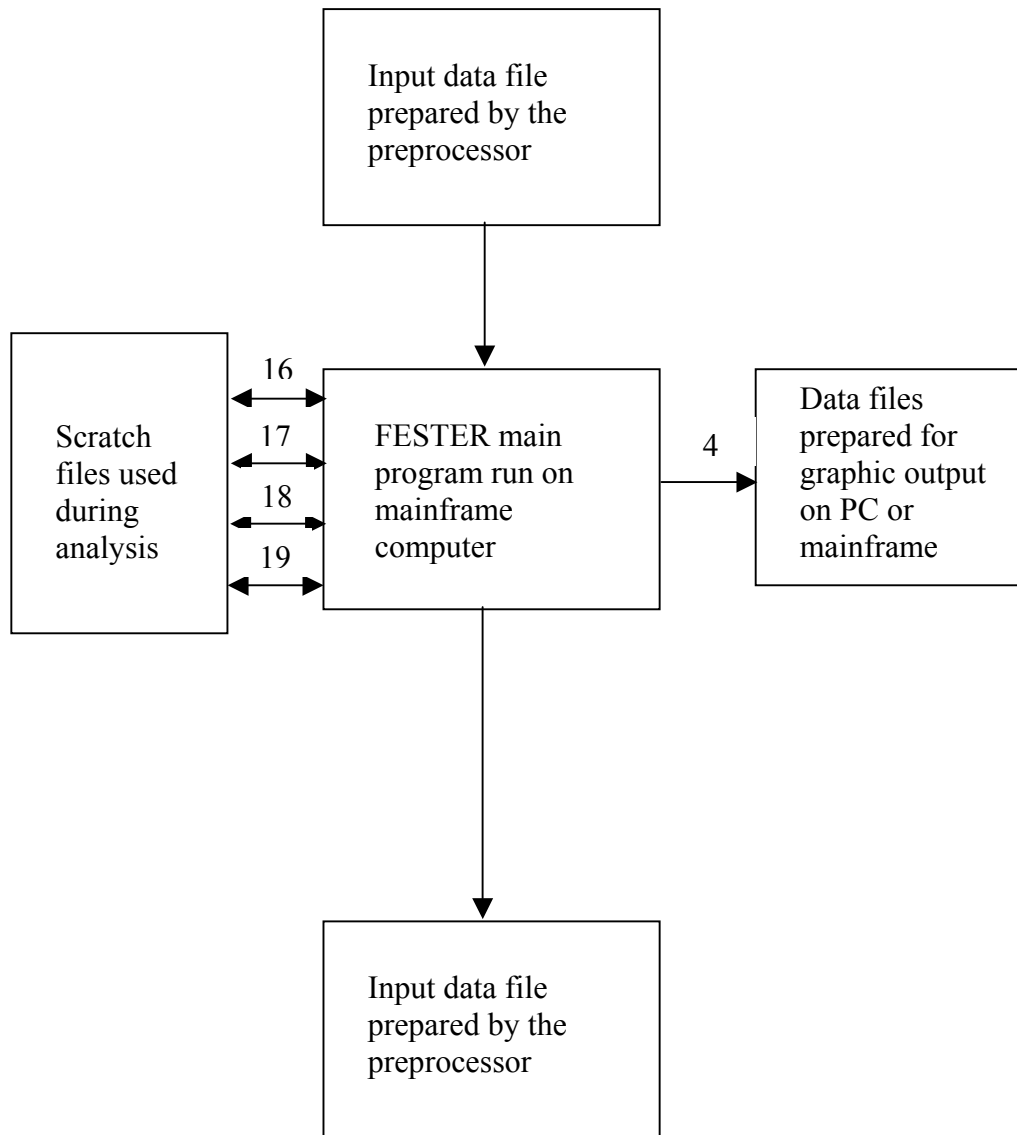


Figure 2.2 FESTER main program system.

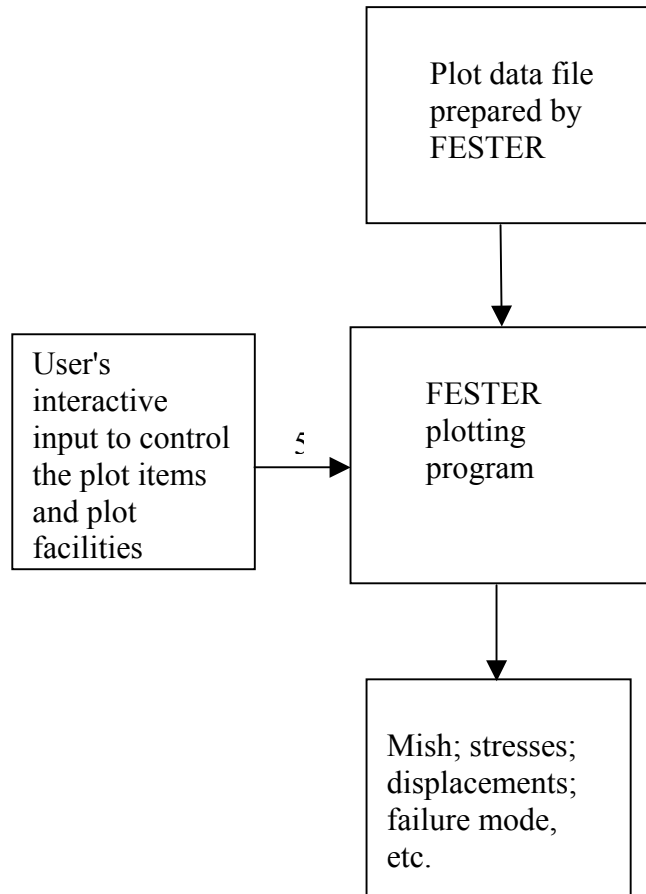


Figure 2.3 Post-processor system.

3 Descriptions of some new features

This chapter describes briefly some of the new features which were not mentioned in the previous report (Reed and Lavender 1989).

3.1 The large deformation analysis

For the large deformation analysis (option NLAPS=2) in the program, the strain-displacement relation is defined as:

$$\{\epsilon\} = \begin{Bmatrix} \epsilon_x \\ \epsilon_y \\ \epsilon_{xy} \end{Bmatrix} = \begin{bmatrix} \frac{\partial u_n}{\partial x} + \frac{1}{2} \left(\frac{\partial u_n}{\partial x} \right)^2 + \frac{1}{2} \left(\frac{\partial u_n}{\partial x} \right)^2 \\ \frac{\partial u_n}{\partial y} + \frac{1}{2} \left(\frac{\partial u_n}{\partial y} \right)^2 + \frac{1}{2} \left(\frac{\partial u_n}{\partial y} \right)^2 \\ \frac{\partial u_n}{\partial x} + \frac{\partial u_n}{\partial y} + \frac{\partial u_n}{\partial x} \frac{\partial u_n}{\partial y} + \frac{\partial u_n}{\partial x} \frac{\partial u_n}{\partial y} \end{bmatrix}. \quad (3.1)$$

Where $\epsilon_x, \epsilon_y, \epsilon_{xy}$, are the shear components in x,y plane and u_n, v_n are the displacements at time t_n .

The incremental equilibrium equation is

$$\int_{\Omega} B^T \Delta \sigma^n d\Omega + \int_{\Omega} B_{nl} \sigma^n d\Omega - \Delta f^n = 0 \quad (3.2)$$

and the global stiffness matrix is

$$K^n = K_1^n + K_{ll}^n = \int_{\Omega} B^T \hat{D} B d\Omega + \int_{\Omega} G^T M^n G d\Omega + \quad (3.3)$$

where M is a matrix involving the current state of stresses and G is a matrix involving shape function derivatives similar to B (Pan 1988). With the above formulations, nodal co-ordinates are updated in the time stepping iterations and the load should be applied in small incremental steps. A problem of a cantilever undergoing large deformation as shown lay Pan (1988) has been tested using FESTER and results are satisfactory.

3.2 Axisymmetric analysis

With the original program structure, the axisymmetric formulations have been implemented in **FESTER**. In accordance with the plane strain analysis, the stress and strain vector are arranged as

$$\sigma = \{\sigma_r, \sigma_z, \sigma_{rz}, \sigma_\theta\} \quad (3.4)$$

and

$$\epsilon = \{\epsilon_r, \epsilon_x, \epsilon_{rx}, \epsilon_\theta\} \quad (3.5)$$

where r, z, θ are radial, axial and tangential co-ordinates respectively, the related matrix such as D, B, G in equation (3.3) have to be arranged in the same fashion. Several circular tunnel problems have been tested using the axisymmetric analysis against the plane strain solution and the results proved to be identical.

3.3 A new way of simulating excavation

In the original **FESTER**, the excavation process was numerically simulated by applying the equivalent nodal forces in opposite directions on the tunnel boundary. Apart from the lack of realistic physical meaning, it is also very difficult to use this method to simulate progressive excavations of different areas.

A new method called 'stress and stiffness reduction method' (Pan 1988, Pan et al 1989) has been adopted in **FESTER**. In the method, all the elements to be excavated will be kept in the analysis (acting as 'ghost elements' after excavation). Excavation starts with reduction of stresses in the excavated elements, which is closer to the real excavation process. This will disturb the established equilibrium at the time step t^n and gives an out-of-balance force as

$$\Gamma^n = \int_{\Omega} B^T \sigma_{exv}^n d\Omega + f^n \neq 0 \quad (3.6)$$

Where $\sigma_{exv}^n = \alpha \sigma^n$ and α is an excavation factor. The excavation induced displacements are therefore calculated as

$$\delta d^n = \left[\int_{\Omega} B^T D_{exv}^n B d\Omega \right]^{-1} \Gamma^{-1} \quad (3.7)$$

where $D_{exv}^n = \alpha D^n$ is the reduced stress-strain matrix for the excavated elements and α is the same excavation factor.

The above excavation simulation procedure has been proved effective and convenient. An example of its application is shown in the next chapter (example 3).

4 Application examples

Three examples showing the capabilities of **FESTER** are described in this chapter.....

4.1 Roadway problem in a deep level coal mine

a. Roadway convergence analysis

In longwall coal mining, special gate roads are constructed to service a mining face (Figure 4.1). One of the aims of mining engineering is to protect the roadway opening, that is, to support it in such a way that displacements are kept within operational acceptable limits in a certain period. Thus, an effective means of predicting the distribution of stresses and displacements of the strata around roadway is required.

However, the factors that determine the magnitude of roadway deformation at depth are complex. They include: the in situ stress and the stress redistribution; the strength of roof and floor strata and their failure mode; the geological structure (e.g. discontinuity, anisotropy of bedding planes); the method of excavation and the support method, etc. Currently available finite element packages generally fail to model some of these factors. The program **FESTER** has been specially developed for such types of complex problem.

b. Numerical modeling

Figure 4.2 shows the 2-D finite element mesh representing the problem. The mesh consists of 115 quadrilateral elements including 15 infinite elements. A symmetric condition along the y-axis has been assumed for simplicity. Three types of rock masses are considered in the model.

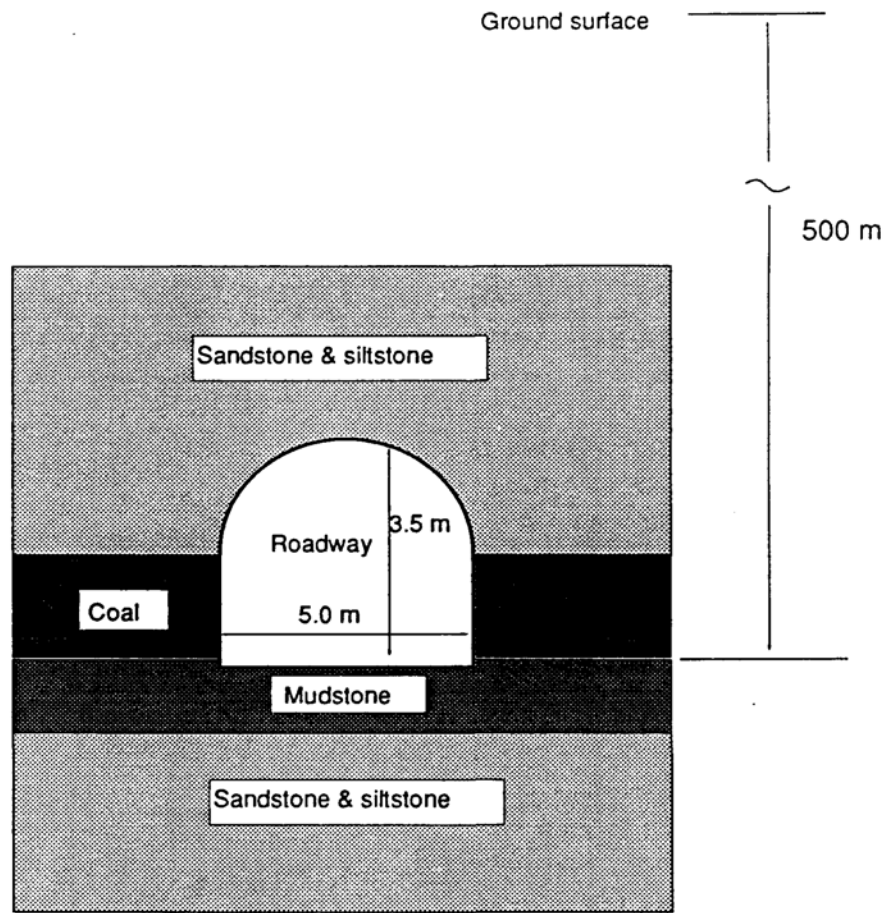


Figure 4.1 A cross section of gate roadways in coal mine.

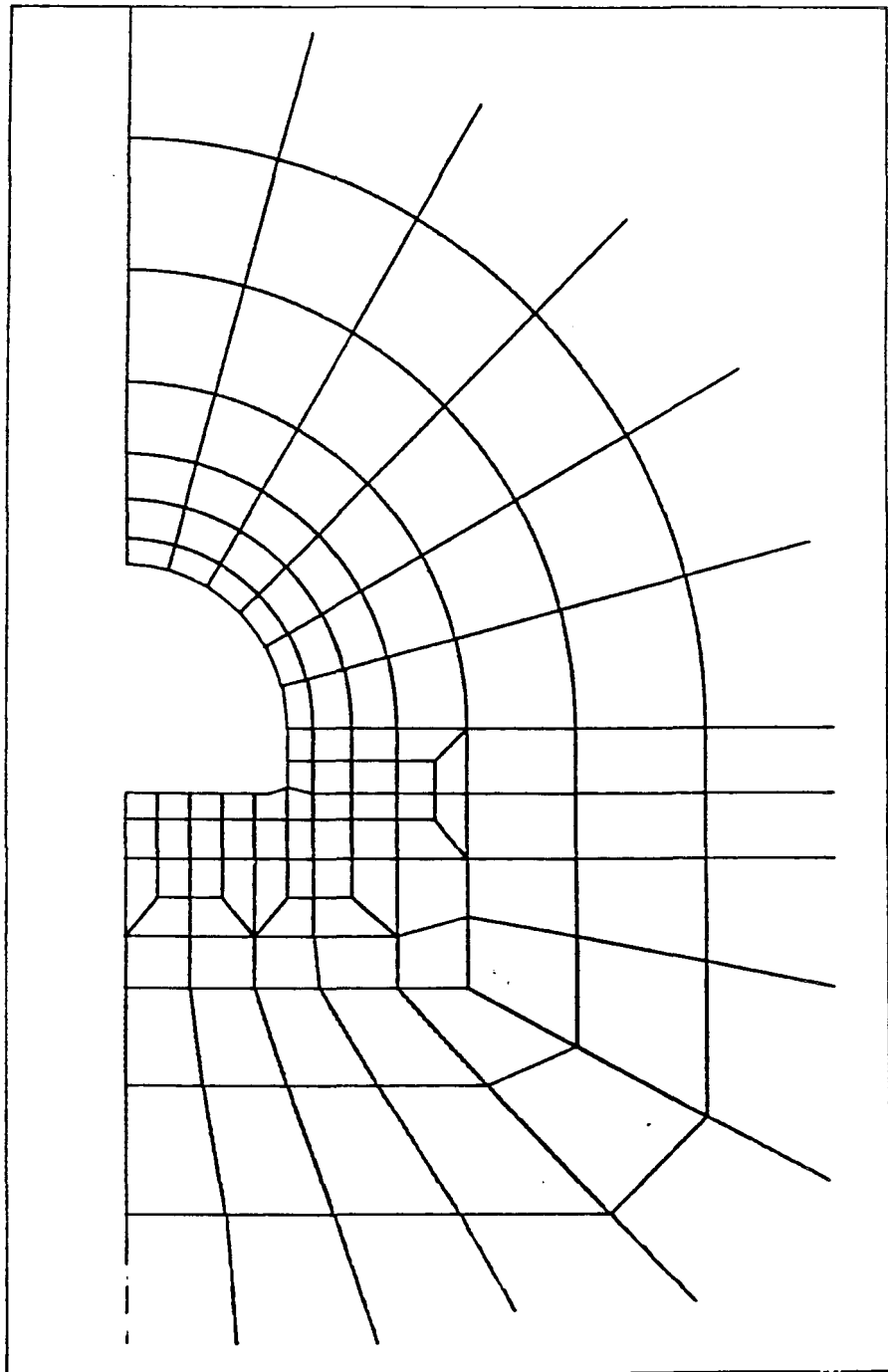


Figure 4.2 Finite element mesh used for the roadway analysis

Isotropic analysis: In the first case, the rock mass properties are assumed isotropic with brittle plastic yield according to the Hoek-Brown strength criterion. Both Drucker-Prager and Hoek-Brown failure rule have been tested with dilation varying from large (close to associated flow) to zero. Applied *in situ* stress ratio ($k_0 = \sigma_v / \sigma_n$) is in a range of 0.8 to 1.2. The material parameters are chosen from data provided by British Coal. The data are then correlated to the empirical strength parameters using the updated Hoek-Brown criterion (Hoek and Brown 1988). In the model, the 'undisturbed' rock mass parameters m, s are used as peak strength parameter and the 'disturbed' rock mass parameters m', s' are used as residual strength parameter. A typical set of rock parameters used in the analysis are shown in Table 4.1. An implicit time stepping algorithm is used with $\theta=0.667$. The excavation of the roadway is modeled by applying opposite nodal forces at the tunnel boundary in 4 steps. In this isotropic analysis, the influence of *in situ* stress, the rock mass strength and their post failure behaviour on the roadway deformation are investigated.

Orthotropic analysis: the model is then changed to take account of the influence of anisotropic behaviour and weak bedding planes. The elastic Young's modulus in the vertical direction is assumed to be only half of the horizontal one. A representative set of parameters used for the anisotropic analysis (laminated rock mass with different strength at bedding planes) is shown in Table 4.2. It is noted from the table that other rock mass properties are chosen identical to that of Table 4.1. Therefore, the influence of the bedding plane strength and the orthotropy on the stress and deformation is investigated.

Computing results

A series of analyses have been carried out in which the finite element mesh was kept the same while the material properties and *in situ* stress field were varied. Only a limited number of results are chosen here to illustrate the program capabilities.

Parameters	Rock Type 1 (Sandstone & Siltstone)	Rock Type 2 (Coal seam)	Rock Type 3 (Mudstone)
E	10000 MPa	3500 MPa	9000 MPa
V	0.25	0.30	0.25
σ_c	40 MPa	25 MPa	30 MPa
M	8.78	2.865	2.40
S	0.189	0.0205	0.015
m'	5.14	0.0821	0.70
S'	0.082	0.00293	0.0025
α	0.015	0.015	0.015
α_1	0.1 MPa	0.06 MPa	0.06 MPa
<p>Average rock mass density = 0.025 MN/m³. <i>in situ</i> stress ratio: k=0.8 --1.2.</p>			

Table 4.1 Material parameters (isotropic) used in one of the simulations.

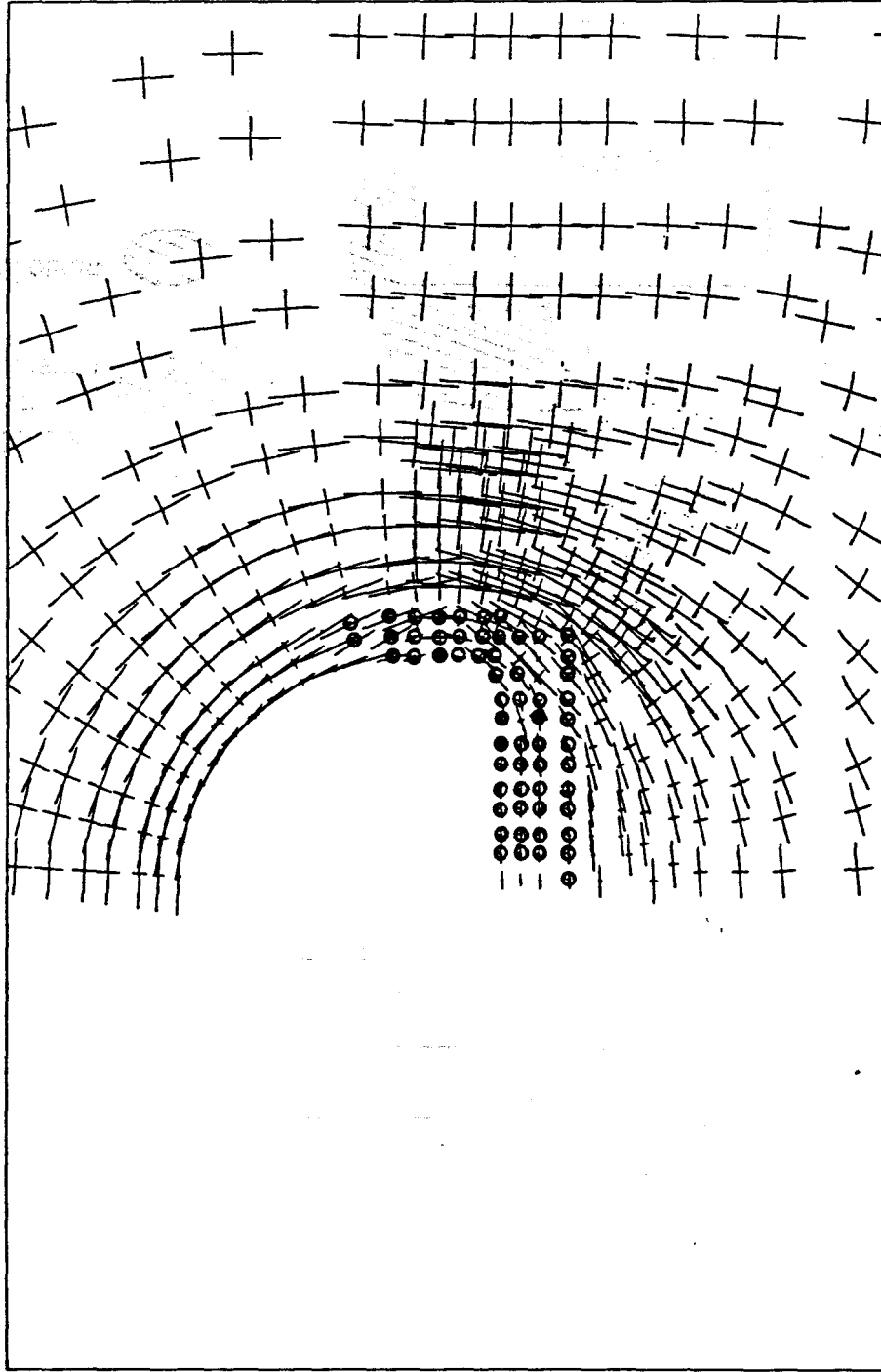
Parameters	Rock Type 1 (Sandstone & Siltstone)	Rock Type 2 (Coal seam)	Rock Type 3 (Mudstone)
E_1	10000 MPa	3500 MPa	9000 MPa
ν_1	0.25	0.25	0.25
σ_c	40.0 MPa	25 MPa	30 MPa
E_2	5000 MPa	1750 MPa	4500 MPa
ν_2	0.30	0.30	0.30
G	3500 MPa	1250 MPa	3200 MPa
M	8.78	2.865	2.40
S	0.189	0.0205	0.015
M'	5.14	0.0821	0.70
s'	0.082	0.00293	0.0025
α	0.015	0.015	0.015
γ	0.01	0.01	0.01
ϕ_j	20.0	20.0	20.0
C_j	2.0	2.0	2.0
ψ_j	0.015	0.015	0.015
γ_j	0.001	0.001	0.001
σ_1	0.1 MPa	0.06 MPa	0.06 MPa
<p>Average rock mass density = 0.025 MN/m³. <i>in situ</i> stress ratio: k=1.2.</p>			

Table 4.2 Anisotropic material parameters used in one of the simulations.

Stresses and failure zones: Figure 4.3 is a computer plot of the calculated principal stresses and failure zone using the material properties shown in Table 4.1. The *in Situ* stress ratio in this case is $k_0 = 0.8$. The brittle failure zone (indicated by circled stress points) occurs only in the coal seam and floor stratum due to the relatively high strength of the roof stratum and the arch-shape roof. The failure mode and the stress distribution along three sections inside the roof, floor and sidewall are shown in Figure 4.4. This prediction is in agreement with the observation of general roadway deformation in British Coal mines where most of the roadway closure is due to the floor lift. Figure 4.5 is plot with the same input data as in Table 4.1 except that the *in situ* stress ratio is chosen as 1.2. This means that the horizontal stress field is increased whereas the vertical stress field remains the same. The predicted failure mode and its stress distribution are highlighted in Figure 4.6.

It is possible that in some particular area, the strengths of the various rock masses around the roadway may be very similar. Figure 4.7 shows results that have been calculated using the coal seam strength parameters for all the rock masses. In that case, the brittle yielding and tensile crack zones are extended into the roof strata, as shown in Figure 4.8.

If orthotropic rock masses are considered, the computed results using the parameters in Table 4.2 are shown in Figure 4.9. There is no failure nor tensile crack in the roof strata although the applied load and other rock properties are identical to the example shown in Figure 4.5 and 4.6. Instead, large shear fracture zones in the roof and floor are predicted. The occurrence of these shear fractures along the horizontal plane of weakness are thought to have released the stress concentration which caused the brittle failure zones in comparison with that of Figure 4.6. If the joint strength is increased from 20MPa , (cohesion $c_j = 2.0$) to 25MPa ($c_j = 3.0\text{MPa}$) the failure mode will be changed significantly to that shown in Figure 4.11. This reveals that the magnitude of the bedding plane strength has a great influence on the roadway stability.



Stresses and failure Zone for $k=0.8$ (H-B cri)
Figure 4.3 Plot of calculated principal stresses and failure Zone

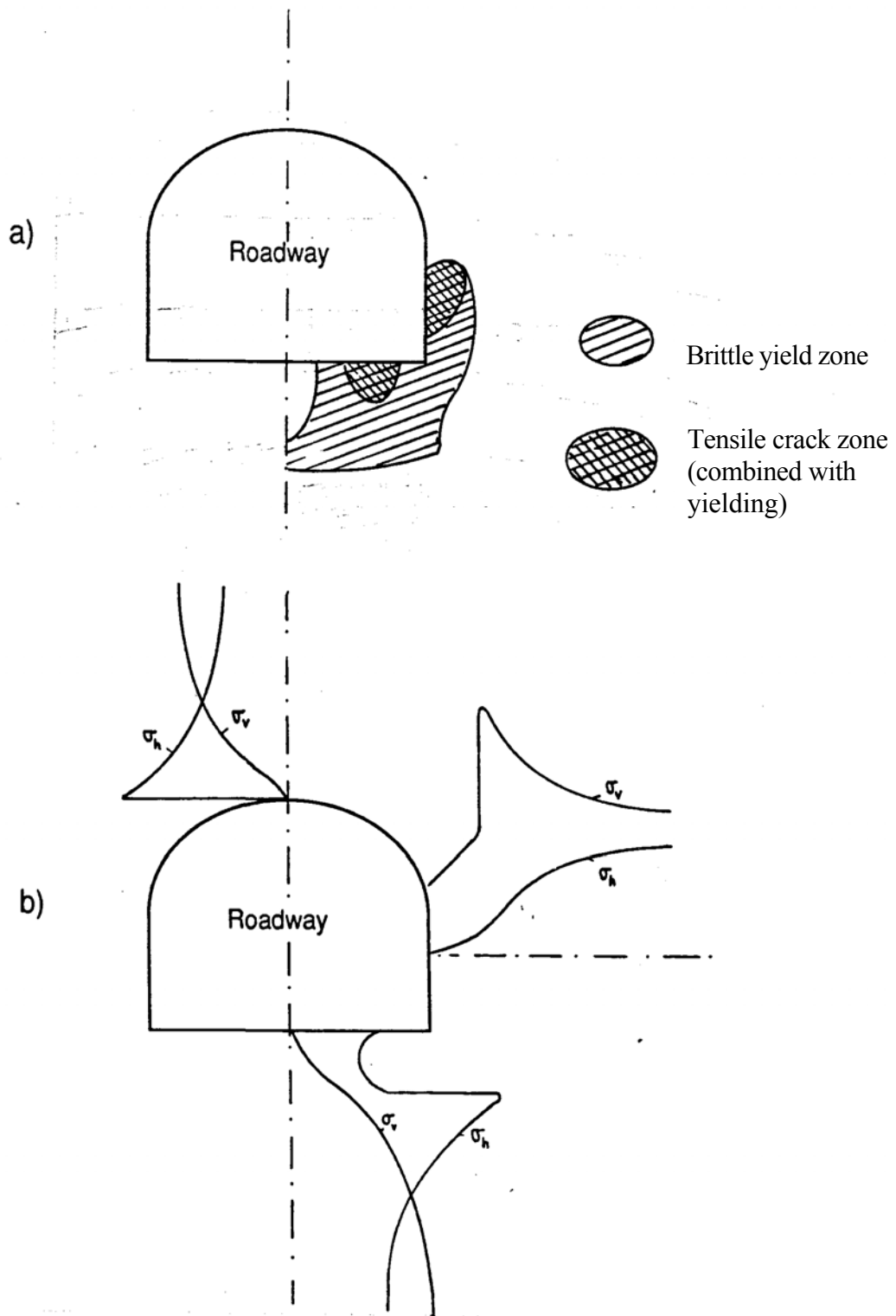
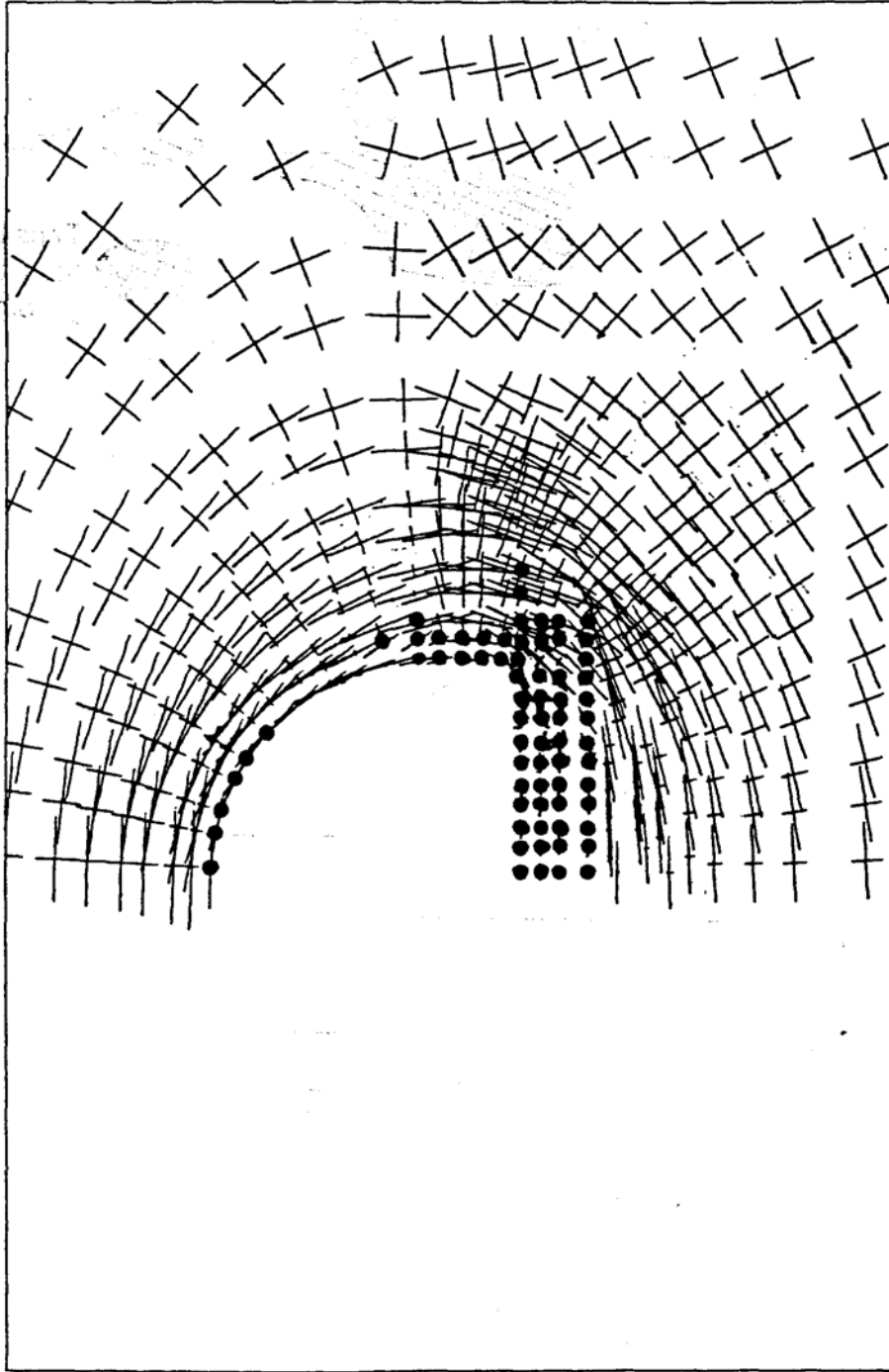


Figure 4.4 Illustration of predicted roadway failure behaviour and stress distributions (stress ratio $k=0.8$).



Stresses and failure Zone for $k=1.2$

Figure 4.5 Plot of calculated principal stresses and failure Zone for high horizontal In situ stress.

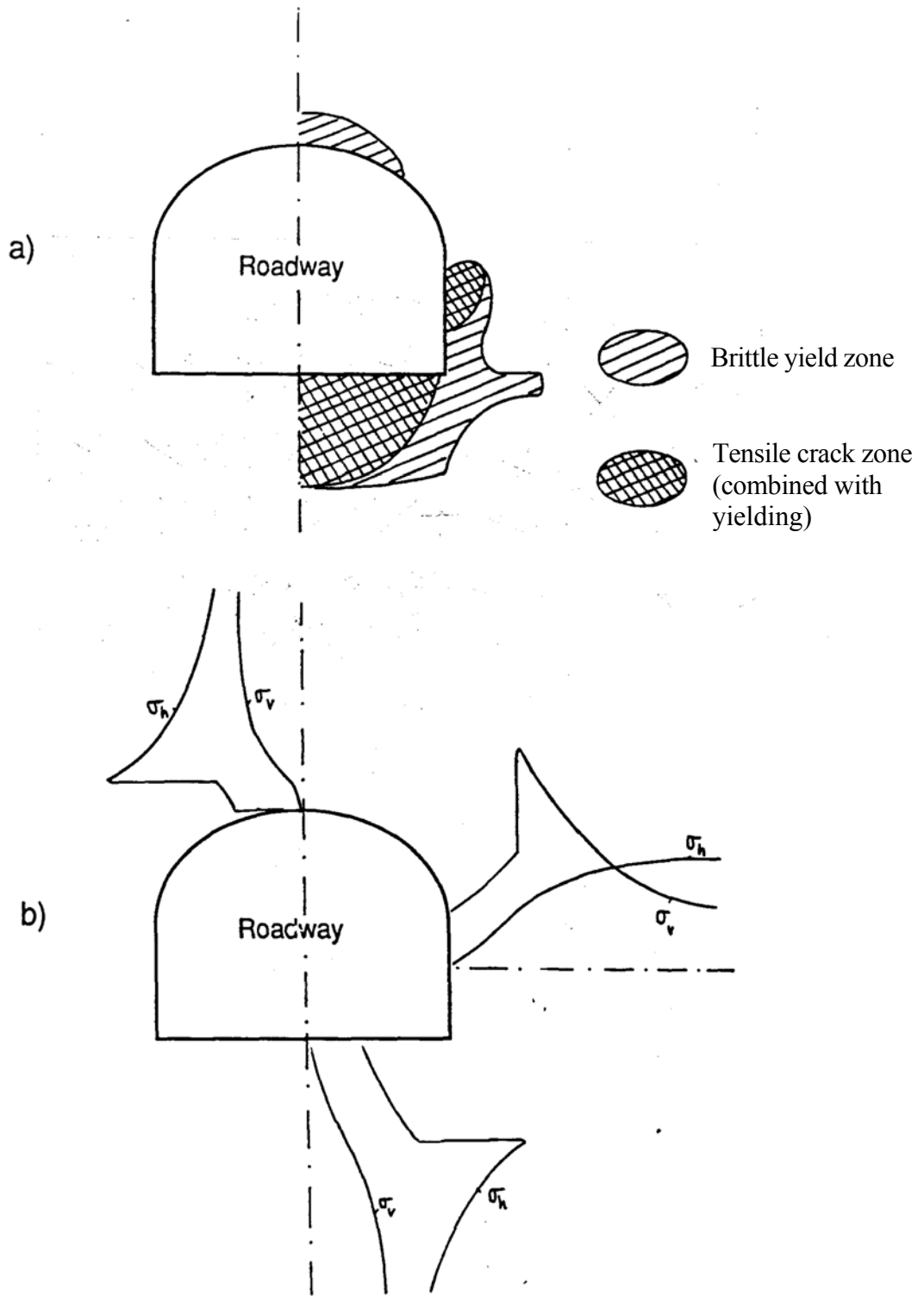
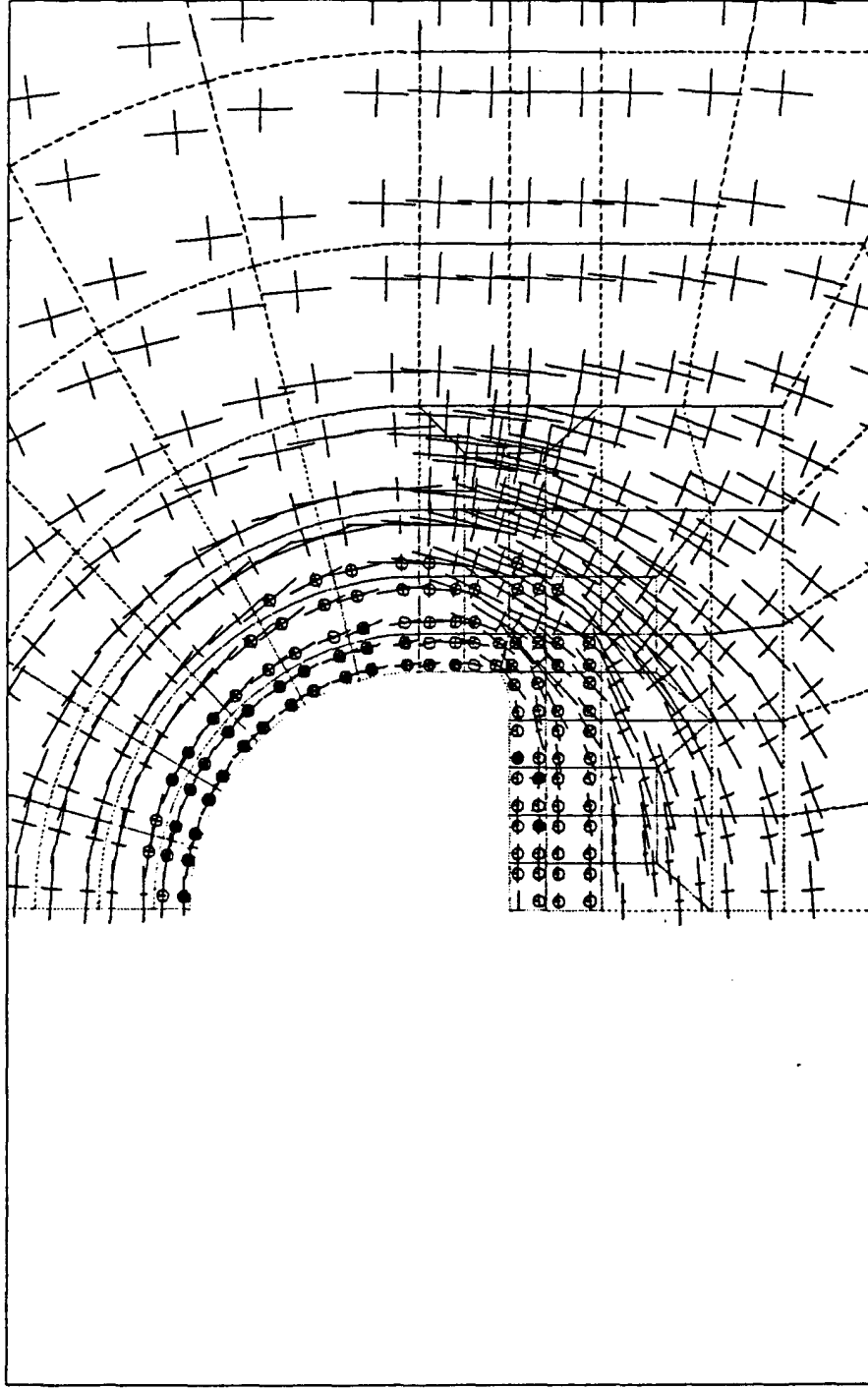


Figure 4.6 Illustration of predicted roadway failure behaviour and stress distributions (stress ratio $k=1.2$).



Cate0 with stress factor $k=0.8$

Figure 4.7 Plot of calculated principal stresses for weak roof strata.

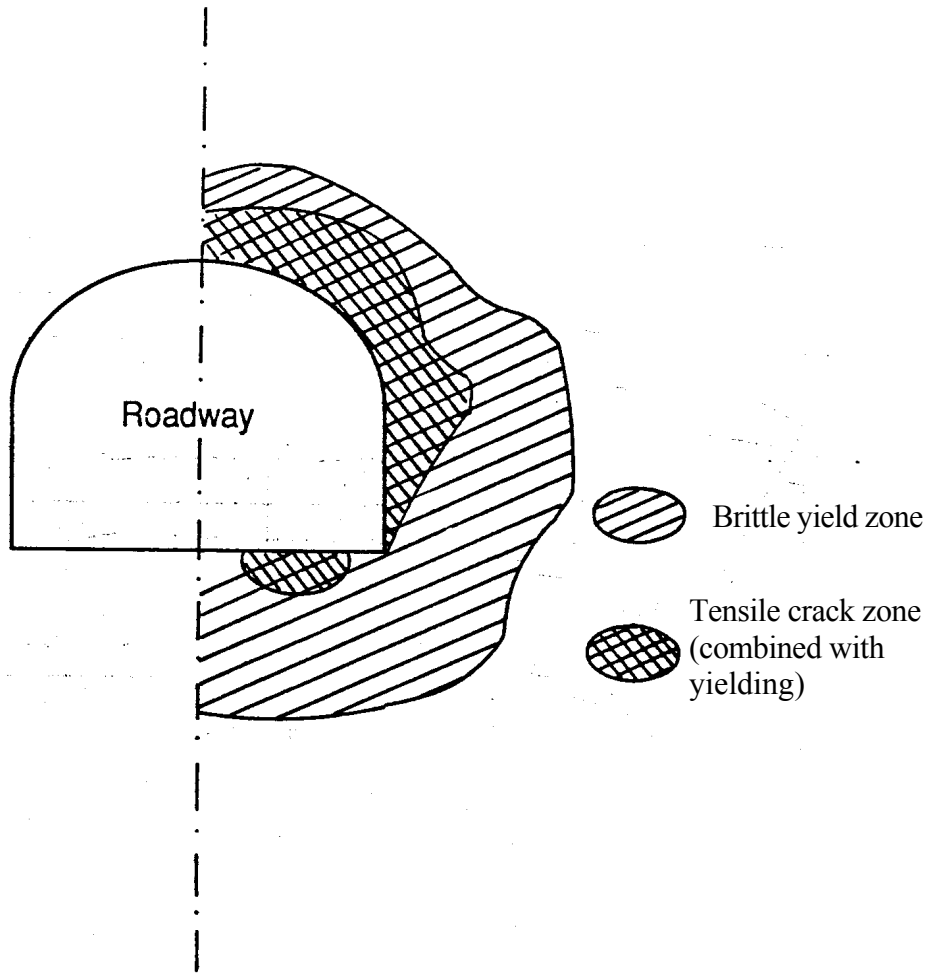
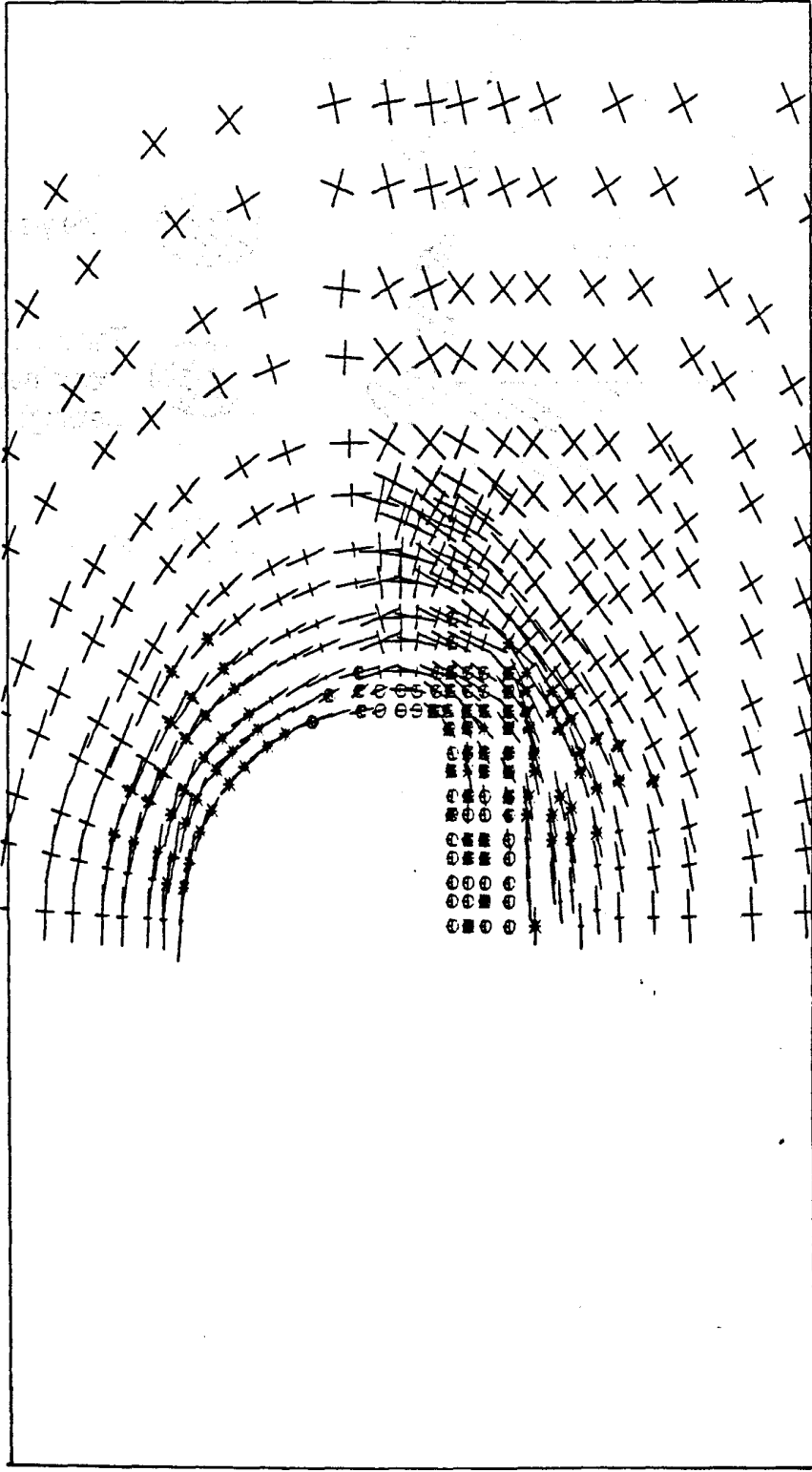


Figure 4.8 The failure zones under weak roof condition (the roof stratum having the same properties as the seam).



Anisotropic anal, with $JC=20.$, $Cj=2.0$

Figure 4.9 Plot of principal stresses and failure zones in anisotropic rock strata (with horizontal shear movements along the joints).

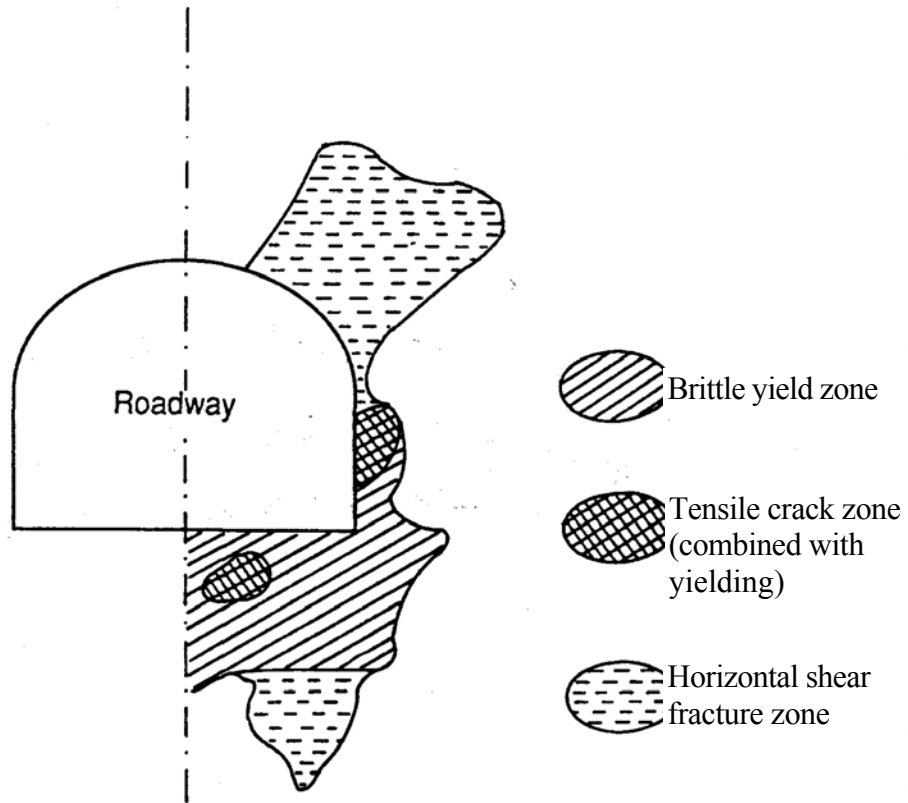


Figure 4.10 Failure zones under anisotropic strata condition (using data of Table 2).

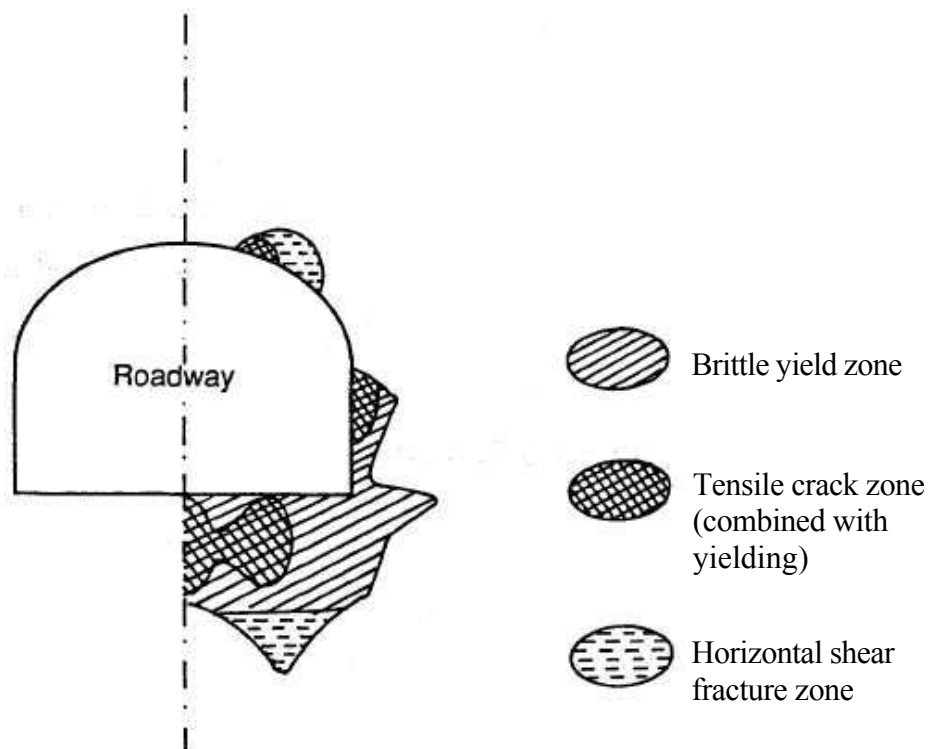


Figure 4.11 Failure zones under anisotropic strata condition with increased horizontal bedding plane strength.

Deformations: A typical mesh deformation plot is shown in Figure 4.12 which corresponds to the analysis of Figure 4.7. The various simulations predict different deformation behaviour. Figure 4.13 illustrates the displacements of roof and floor against the excavation factors (simulating the roadway face advance). In this diagram, all the results have been obtained using identical rock strength properties but with different *in situ* stress ratio. Thus the effect of the *in situ* stress field, the material properties of the rock and the geological structure on the roadway deformations are clear.

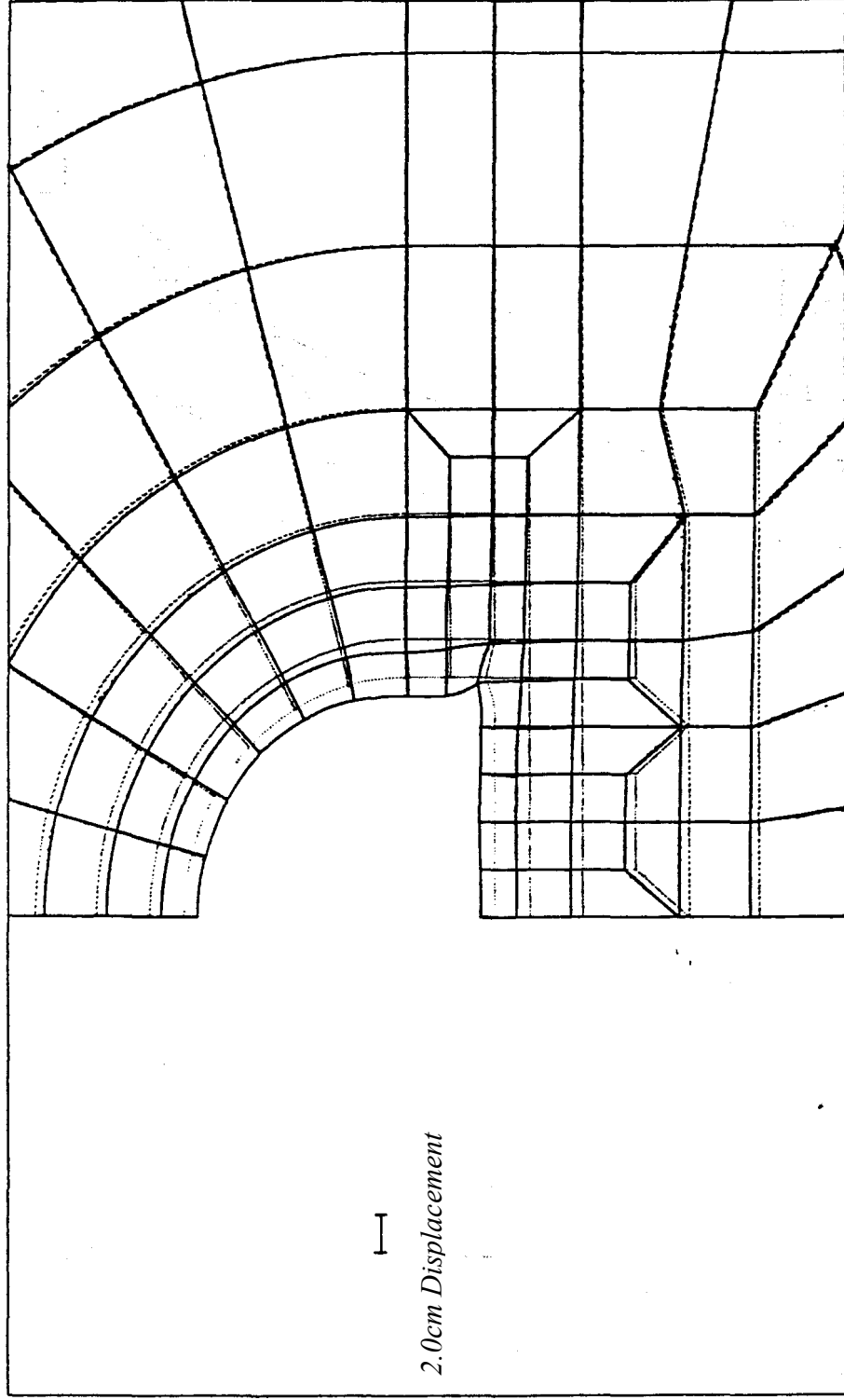
The extent of the roadway deformation appears not as much as that observed in the field. This is because the effects of the longwall face excavation, which is usually the major cause of the roadway closure, is not modelled in this analysis. However, the rock mass behaviour and deformation patterns have been successfully investigated through this model.

4.2 Shallow discharge tunnel stability analysis

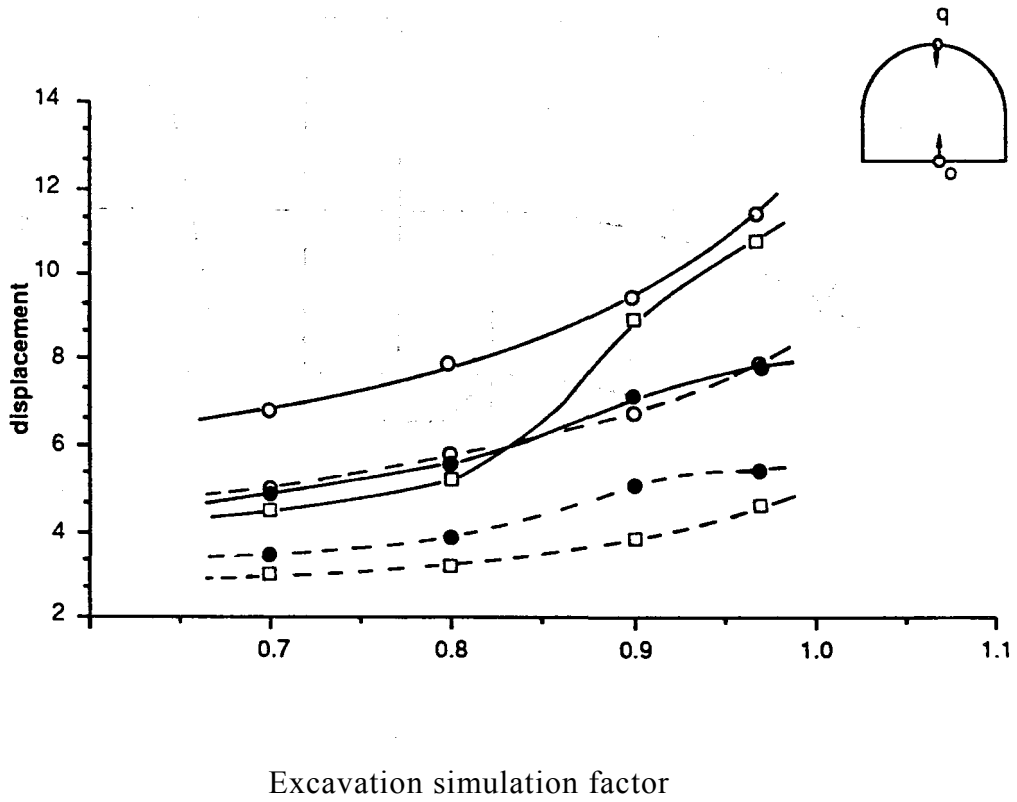
In this section, the application of FESTER as a design tool for reservoir engineering is described.

a. Discharge tunnel problem

In reservoir engineering, discharge tunnels are often excavated for discharge the reservoir when it is necessary. Figure 4.14 shows two perpendicular cross sections of a discharge tunnel problem in Italy. Because the reservoir project is still in a design stage, there have not been any detailed rock or rock mass property data obtained from laboratory or *in Situ* tests. Geological site investigations reported that the rock mass in the area should be classified as class *iii* according to Bieniawski's classification ($RMR = 44$). The tasks facing the design engineers and their consultants are to give an estimation of the require-



Cate0 with stress factor $k=0.8$
Figure 4.12 Plot of mesh deformation (corresponding to the stresses of figure 4.7).



Excavation simulation factor

- Simulation 1: $k_0 = 1.2$
- Simulation 2: $k_0 = 0.8$
- Simulation 3: $k_0 = 0.8$ (anisotropic rock).
- Floor lift (see point o)
- - - - - Roof displacement (point q)

Figure 4.13 Roof and floor displacement vs. excavation simulation factor.

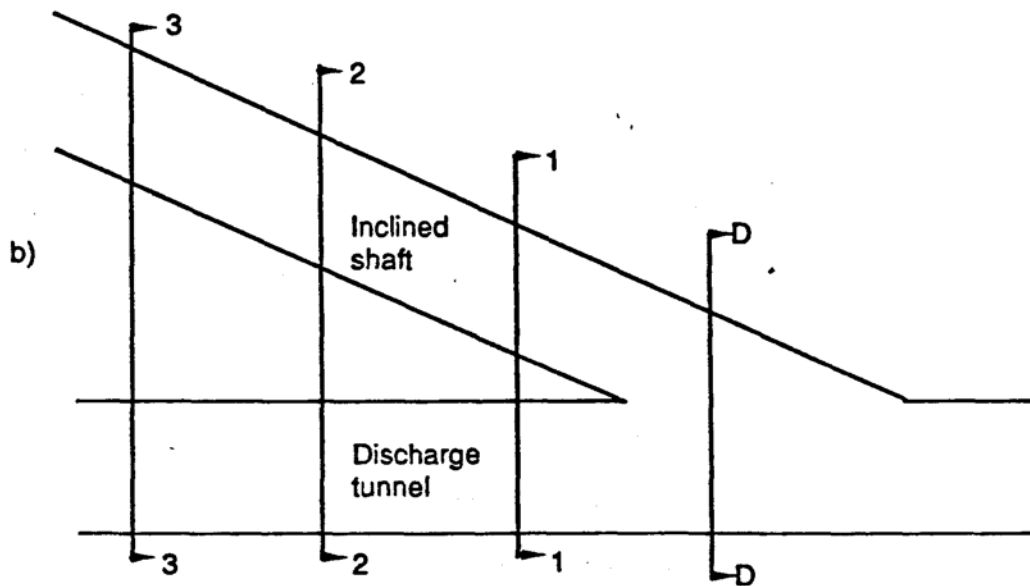
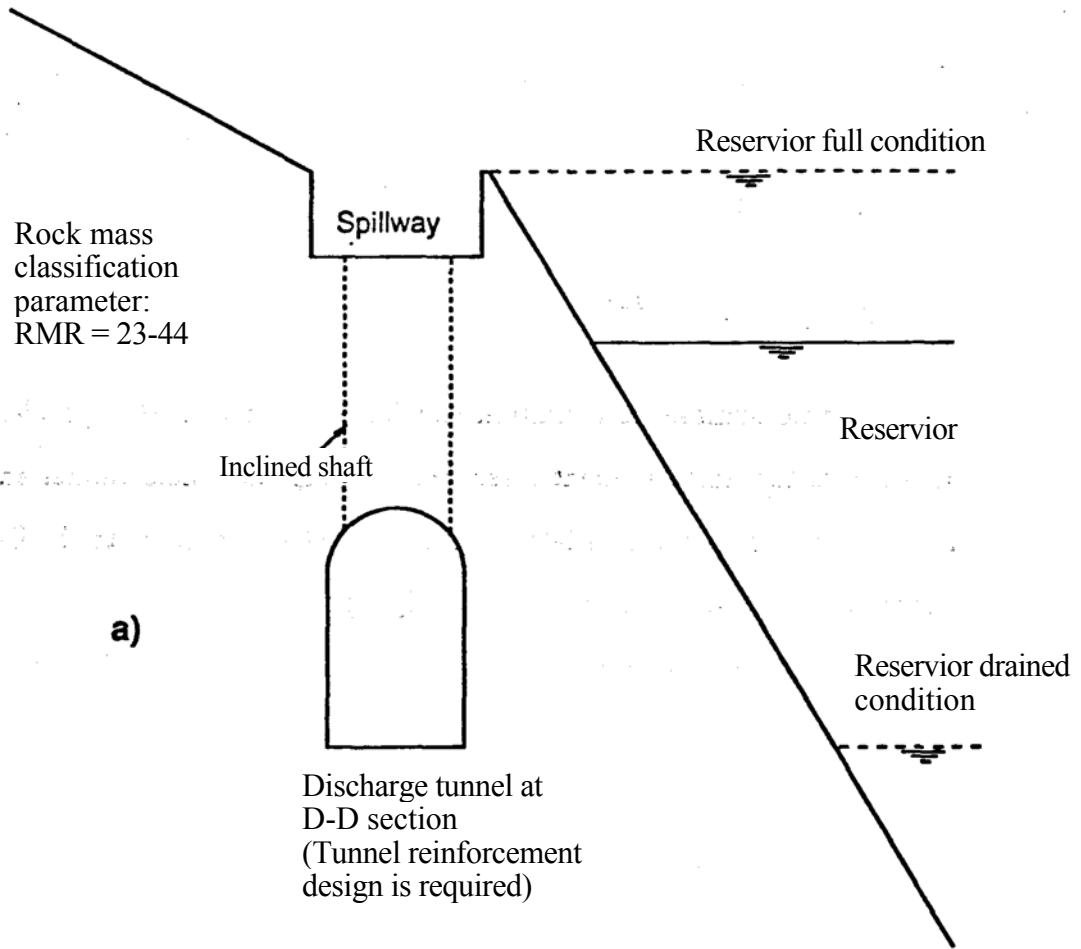


Figure 4.14 A discharge tunnel problem: a) a simplified plane strain section at position D-D; b) A cross section parallel to the tunnel axis.

ments of reinforcement and make an initial tunnel construction design. An elastic analysis is not of much use for the problem. Program FESTER has been used and proved to be an efficient tool for this purpose.

Finite element model

Since no symmetric condition can be considered in this problem, Figure 4.15 shows the finite element mesh representing the whole tunnel and its surrounding rock masses. The 2-D mesh is established according to the D-D section shown in Figure 4.14b (plane strain analysis). 118 elements including 14 infinite elements with 543 nodal points are used in the model. According to the geological survey and design requirements, the boundary conditions of the problem are specified as shown in Figure 4.16. With this mesh, the influence of the shaft at other locations as indicated by Figure 4.14b (3-D effect) can be approximately analysed by excavating the related areas (reducing the stress and stiffness of some elements) in progressive analyses.

Because of the lack of information on the rock mass properties, empirical parameters for the Hoek-Brown criterion are chosen according to the rock mass classification as suggested by Hoek and Brown (1988). The advantage of using the updated Hoek-Brown criterion in FESTER for general rock engineering is well demonstrated by this analysis.

The updated Hoek-Brown criterion gives the empirical parameters for the class iii rock mass (RMR = 44) as:

$$m = 0.947, s = 0.00198 \text{ (for undisturbed rock masses)}$$

$$m' = 0.128, s' = 0.00009 \text{ (for disturbed rock masses)}$$

In this analysis, the undisturbed strength parameters m and s are used for the peak strength criterion and the disturbed parameters m' and s' are used for the residual yield criterion. A uniaxial compressive strength $\sigma_c = 30MPa$ for an intact rock sample is assumed in the analysis. The rock mass density is'

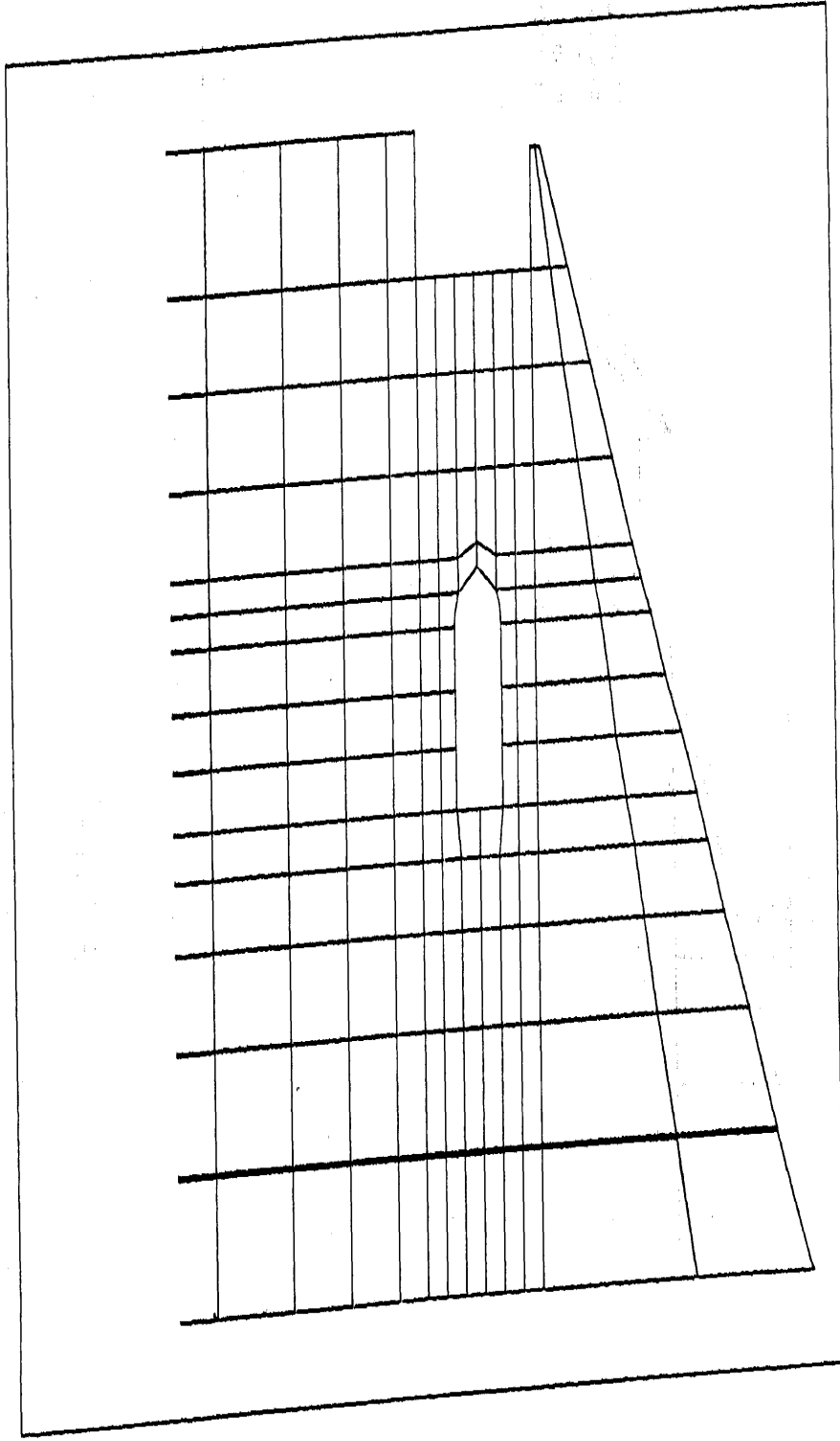


Figure 4 15 Finite element mesh used for discharge tunnel problem.
(118 elements and 543 nodal points).

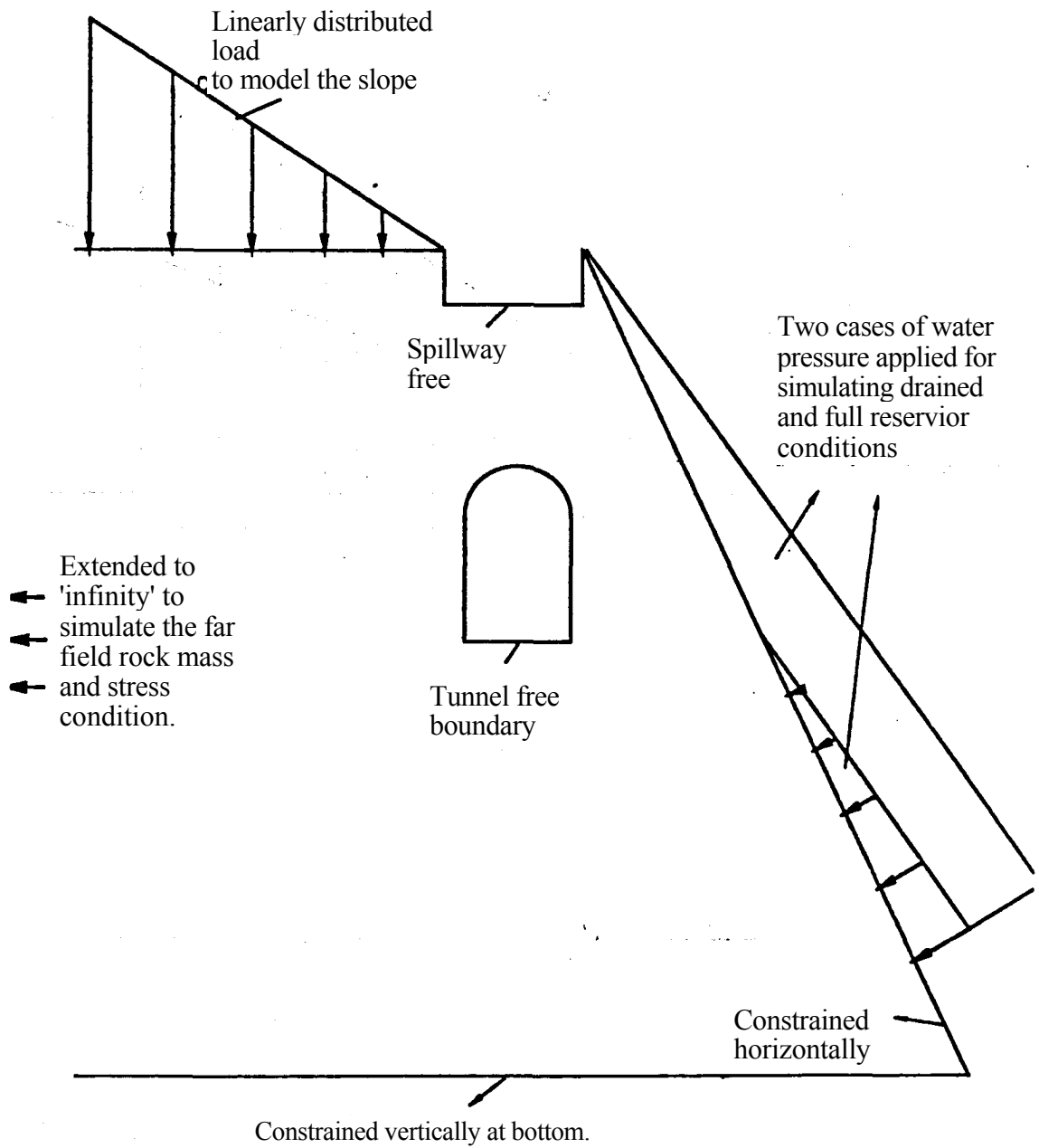


Figure 4.16 The boundary conditions specified in simulating the discharge tunnel problem.

assumed as $2.6t/m^3$. There is no *in situ* stress data available, so only gravity is considered. The horizontal stress is calculated according to a stress ratio k_0 ($k_0 = 0.5 - 1.0$). The effect of the tunnel support is roughly simulated by retaining 10% of the pre-excavation stress along the tunnel boundary.

Results and interpretations

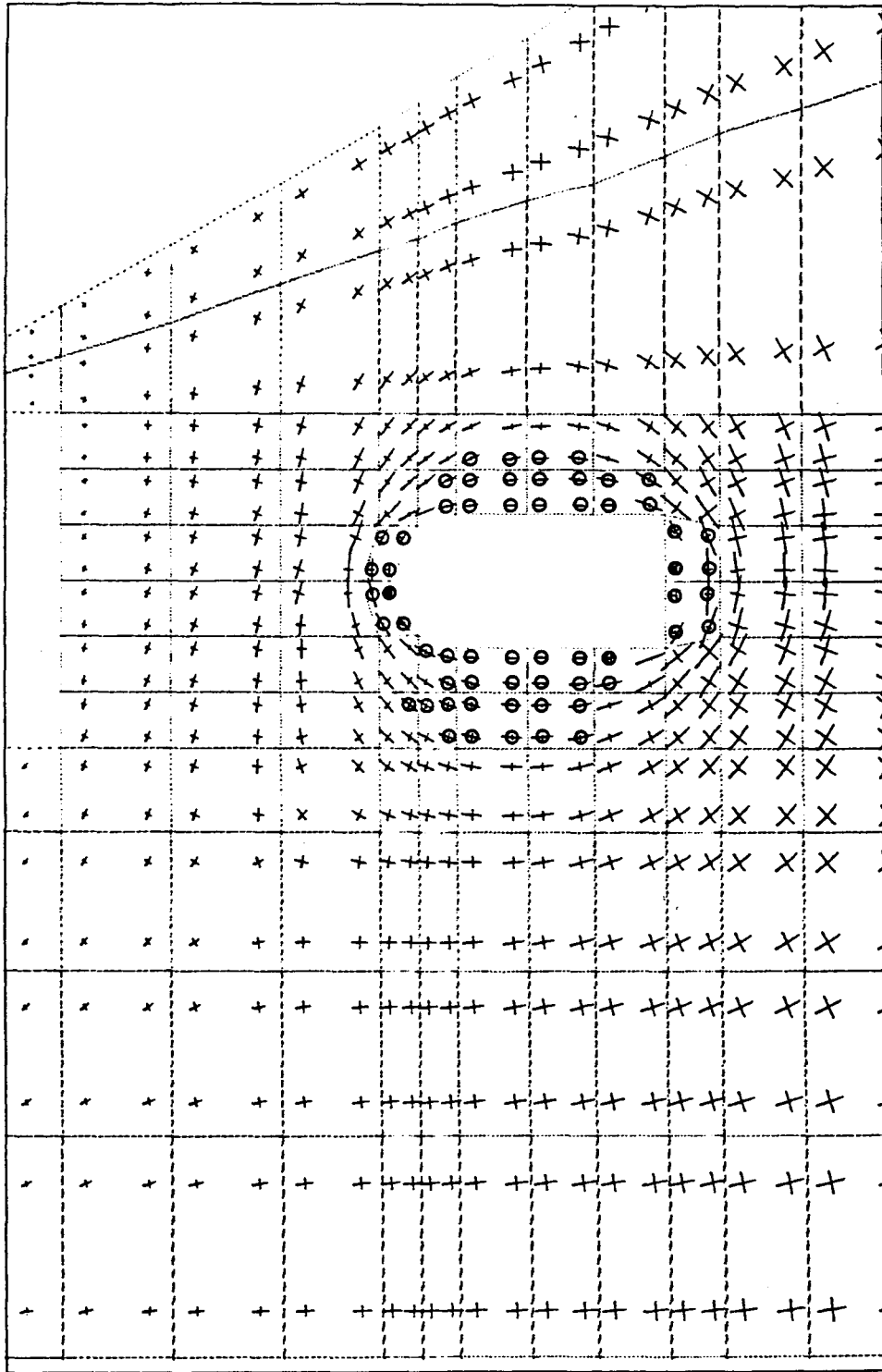
The model predicts that for the 'fair' rock mass ($RMR = 44$) without any support pressure, a failure zone of 6 - 9 meters around the tunnel wall will occur (see Figure 4.17, 4.18). The failure zones near the roof and floor are much lower. The failure zone facing the gorge slope is smaller than on the other side. The effect of water pressure (modelled by distributed boundary load) appears to benefit the stability of the tunnel. For a class *iv* rock mass ($RMR = 23$), the failure zone is predicted to extend close to the bottom of the spillway, which means a collapse of the tunnel would be possible if the tunnel encountered some weak zone such as faults. The tunnel deformation is plotted in Figure 4.20 and a typical stress distribution is shown in Figure 4.21. According to this analysis, a rock bolt reinforcement as shown in Figure 4.22 can be suggested to the designers.

4.3 Progressive excavation of a circular tunnel

In this section, an axisymmetric model of an advancing tunnel face problem using the new excavation simulation method is described.

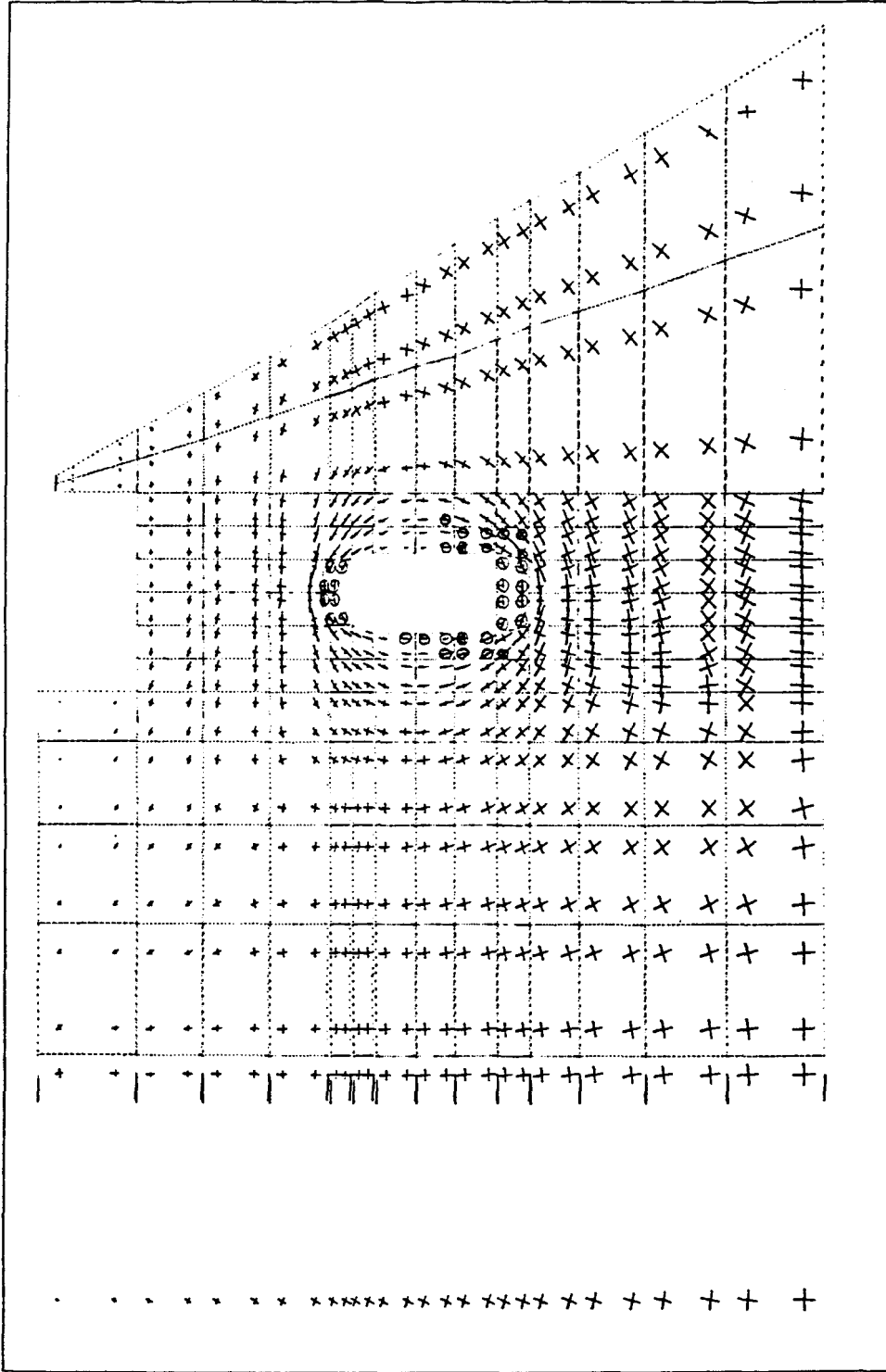
a. Advancing tunnel problem

For a practical 3-D tunnel excavation, the stability and convergence of the tunnel behind an advancing face are of primary interest to designers. The tunnel convergence behind an advancing face is due to the process of excavation



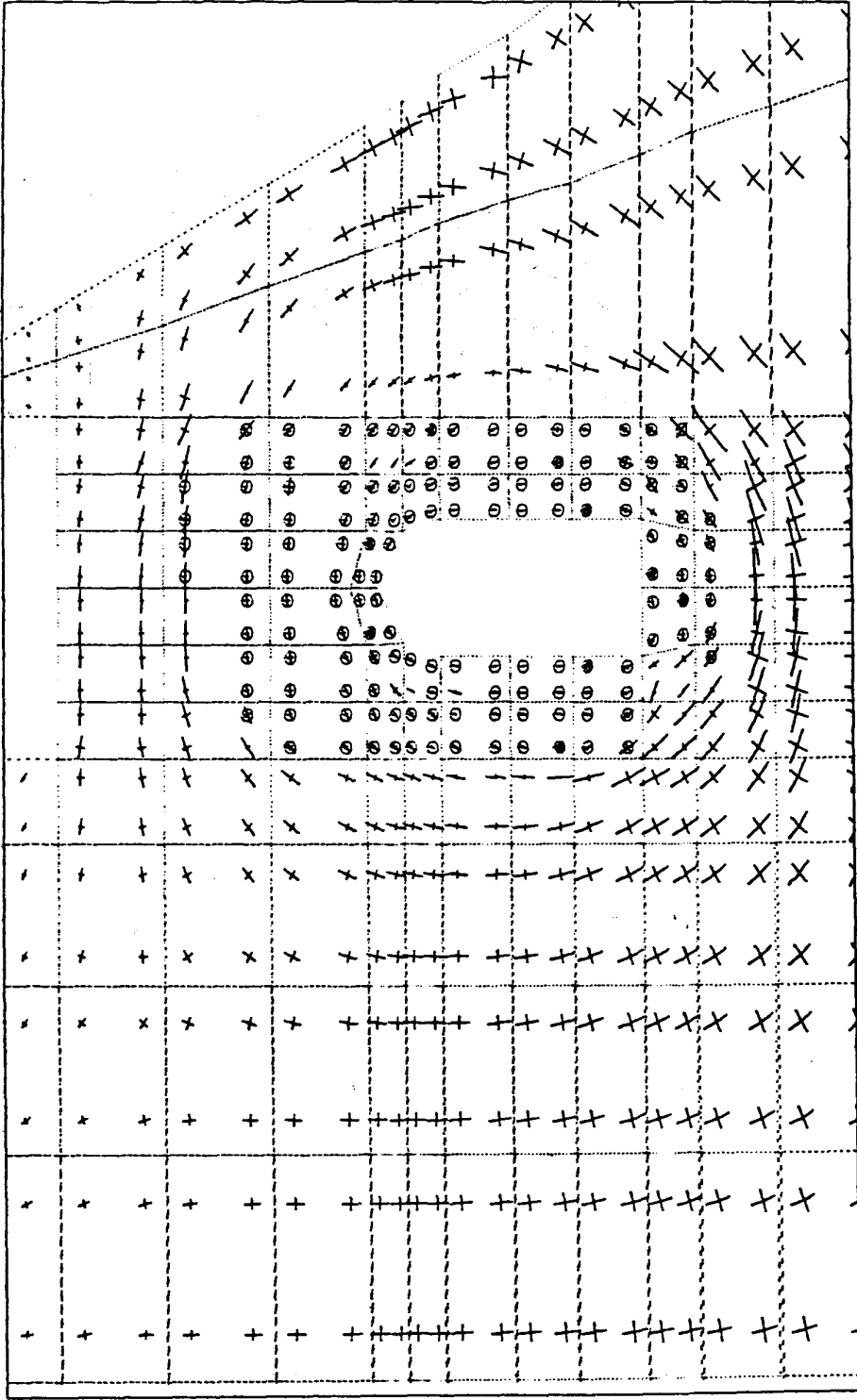
Stress & failure zone for drained condition. (cal. iii)

Figure 4.17 The predicted failure zone under drained reservoir condition.



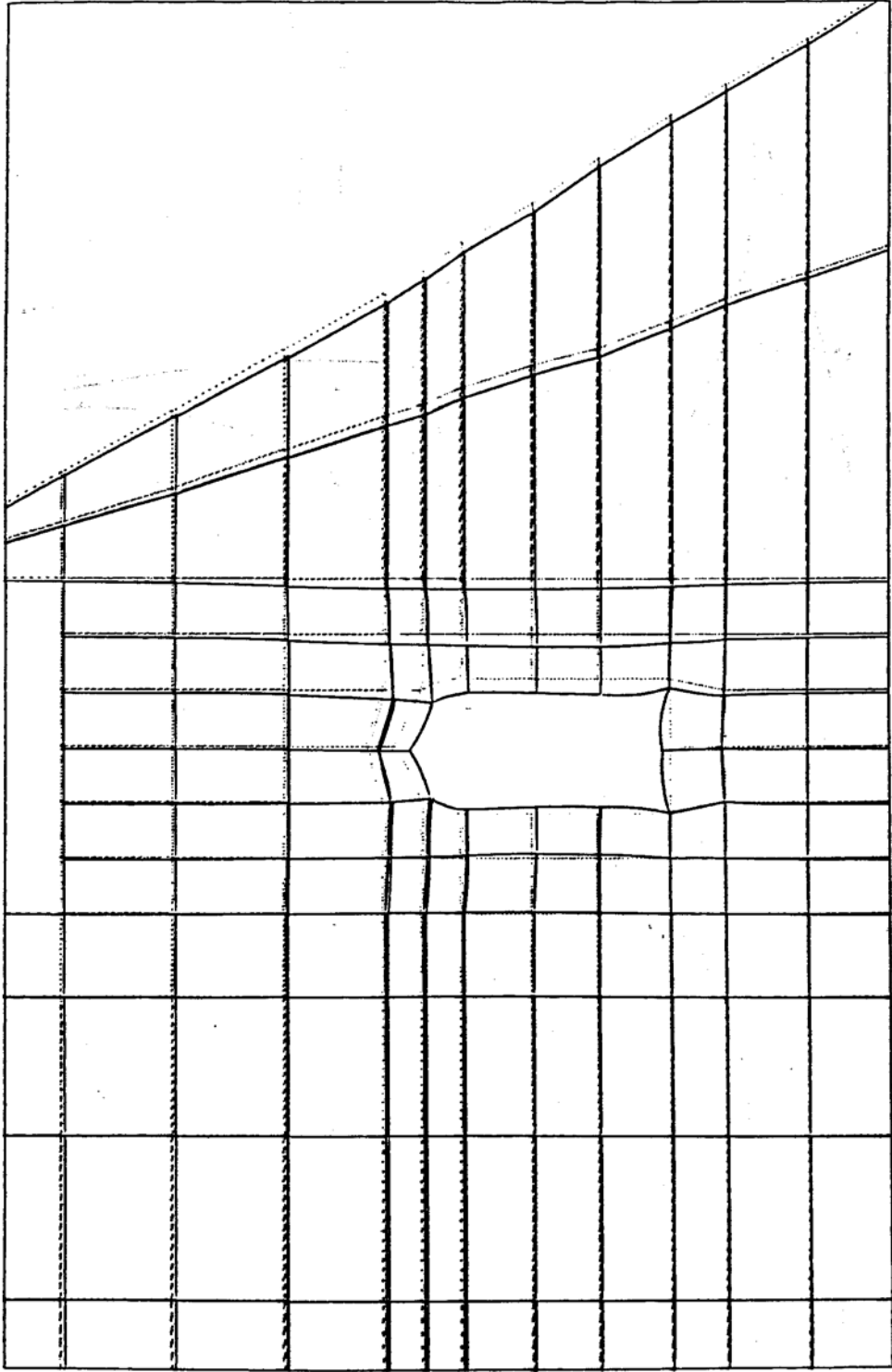
Stress & failure zone for undrained condition. (class iii)

Figure 4.18 The predicted failure zone under full reservoir condition.



Stns. & failure zone for undrained con. (class. iv)

Figure 4.19 The predicted failure zone for class iv rock mass (RMR=23)
Under full reservoir condition.



Predicted tunnel deformation for undrained condition

Figure 4.20 Plot of displacements (magnification factor = 15).

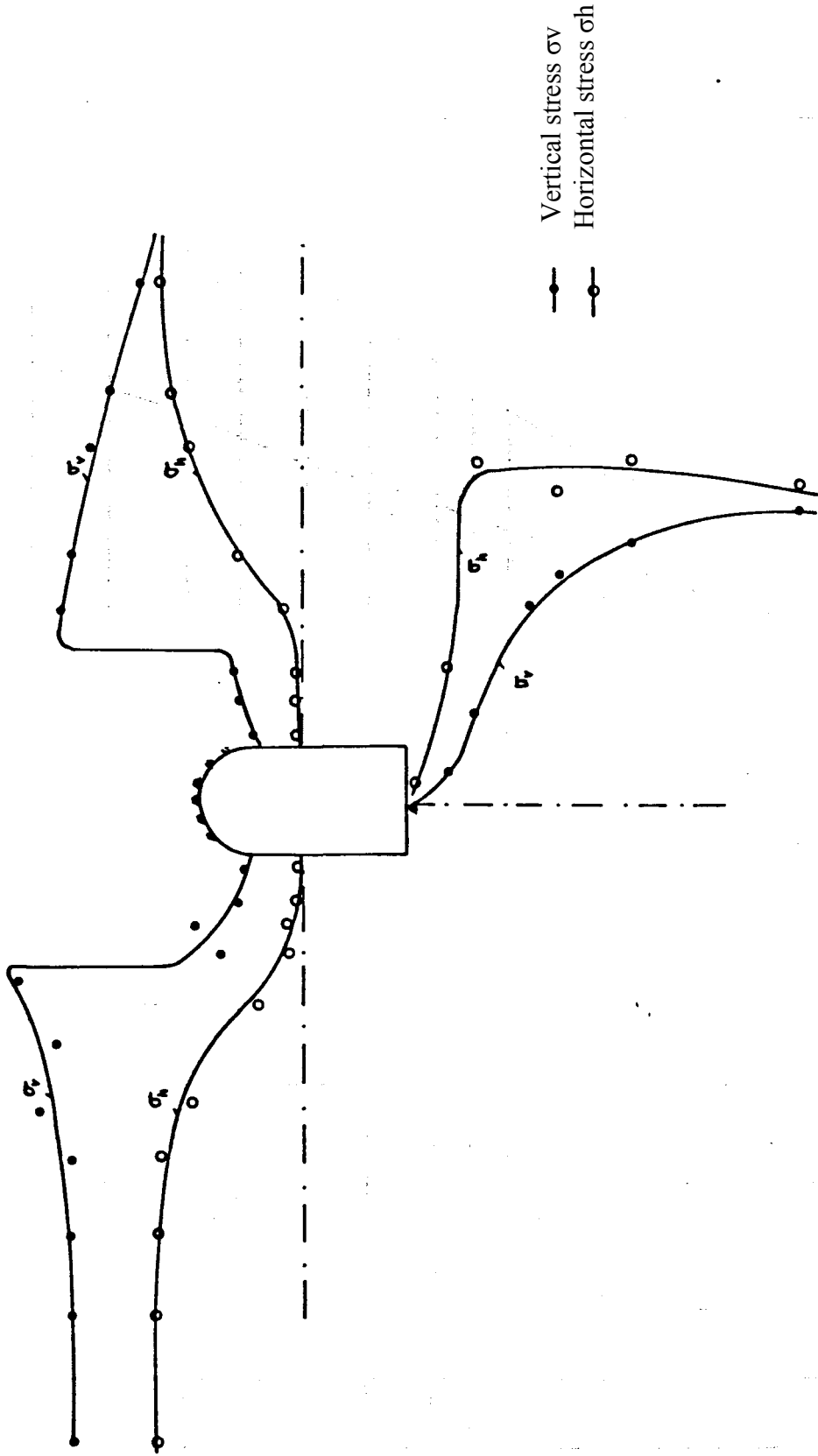


Figure 4.21 The calculated stress distribution around the discharge tunnel.

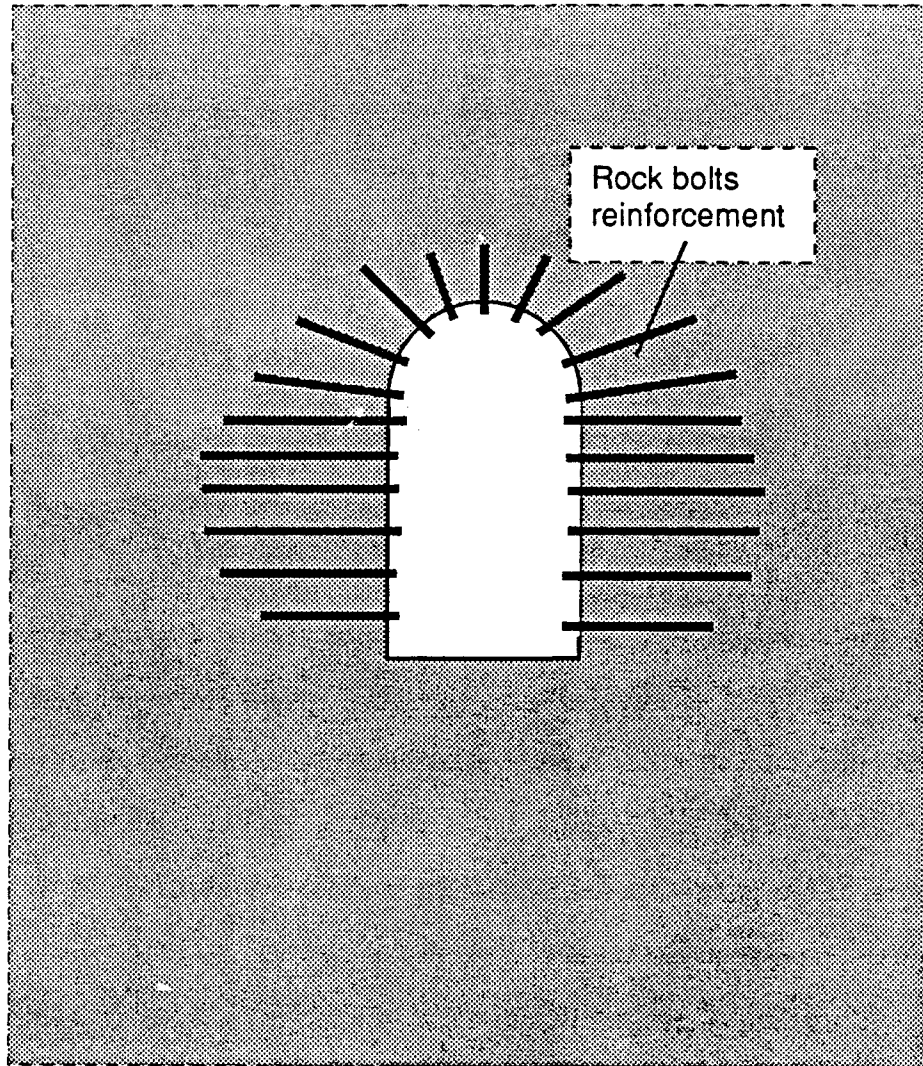


Figure 4.22 The suggested rock reinforcement design according to the analysis of program FESTER.

and the time- dependent behaviour of the rock mass. If a rock mass does not behave elastically, a 2-D plane strain analysis may under-predict the convergence of the tunnel by up to 13 % (Pan and Hudson 1988). This advancing tunnel problem and its 2-D analysis section is shown in Figure 4.23.

b. Numerical modelling

With the existing FESTER, a 3-D circular tunnel advancing problem (under axisymmetric loading condition) can be modelled. The progressive advancement of the tunnel face is simulated by reducing the stress and stiffness of the elements representing excavated rock masses. Figure 4.24 shows the finite element mesh used in the analysis. The mesh consists of 99 elements including 11 infinite elements (315 nodes). Sixteen elements are excavated in 8 steps to model the tunnel face advance. The rock mass is assumed to be an isotropic elastic, brittle plastic medium following the Mohr-Coulomb yield criterion. The main rock properties used are:

$$\sigma_c = 30 \text{ MPa}, k = 3.2, s = 1.0, k' = 1.0, s' = 0.05, \alpha = 0.015 - 0.1$$

A plane strain analysis is also conducted for comparison with the above model.

Results

A predicted axisymmetric principal stress distribution (in σ_r, σ_z plane) is shown in Figure 4.25. It can be seen from the figure that the original *in situ* stress (30 MPa) has been reduced, in 8 steps, to approximately zero in those elements representing the excavated tunnel area. A failure zone is also indicated in the figure. The tunnel boundary deformation behind the advancing face is shown in Figure 4.26 in which a 2-D plane strain prediction is also indicated. A discrepancy of the results between the plane strain analysis and axisymmetric 3-D simulation is obvious. The factors affecting the magnitude of the discrepancy between the plane strain and 3-D analysis are still under investigation using

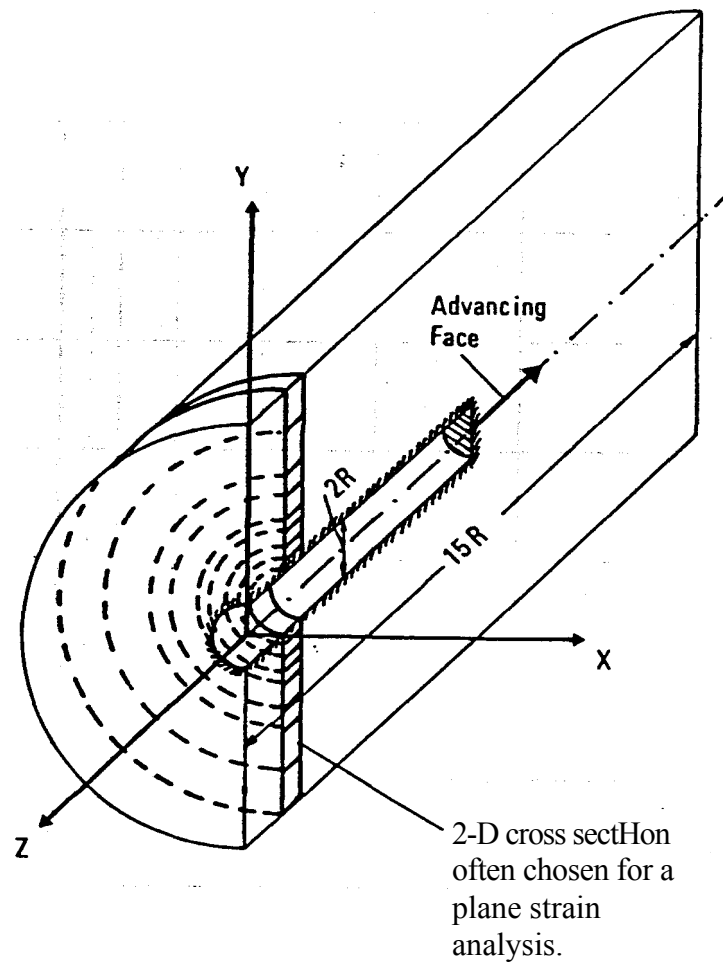
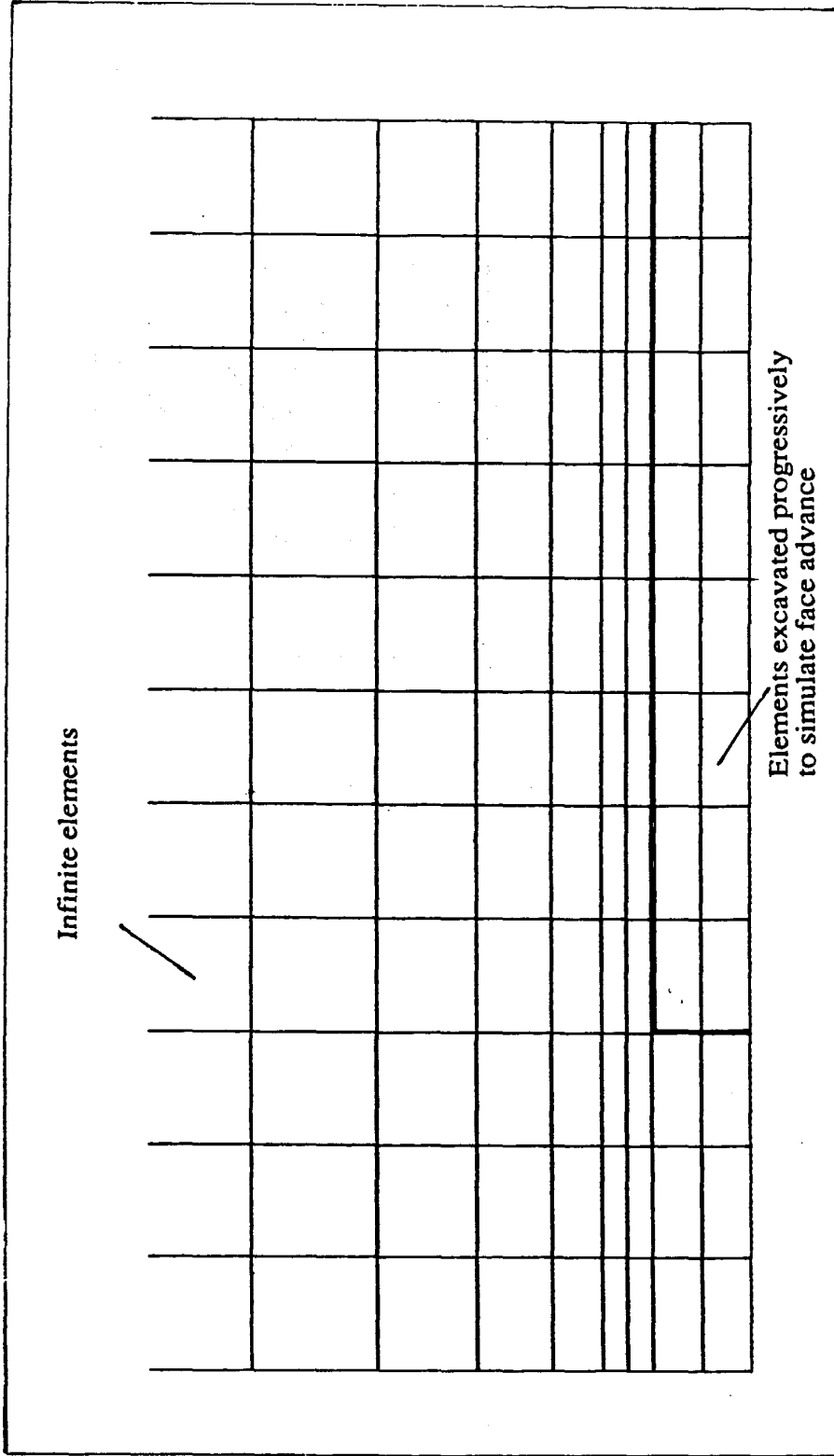
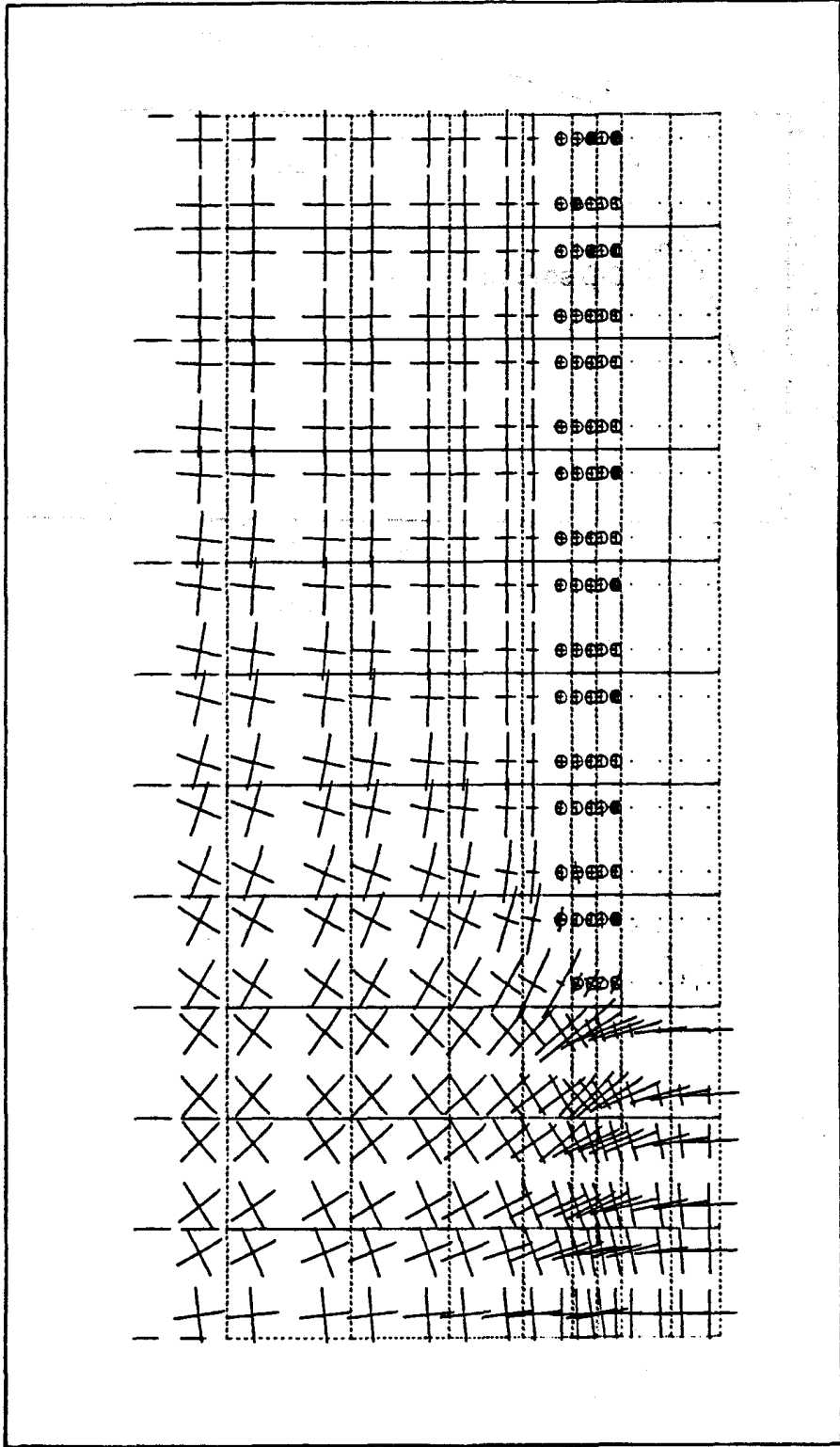


Figure 4.23 Advancing tunnel problem and its plane strain analysis.



Axisymm anal. for 3D excav. ($k' = 1.0, s' = 0.05$)

Figure 4.24 The Axisymmetric finite element mesh used for the advancing tunnel face analysis.



Axisymm anal. for 3D excav. ($k = 1.0, s' = 0.05$)

Figure 4.25 The principal stresses (axisymmetric near the advancing tunnel face (the tunnel was excavated in 8 steps)).

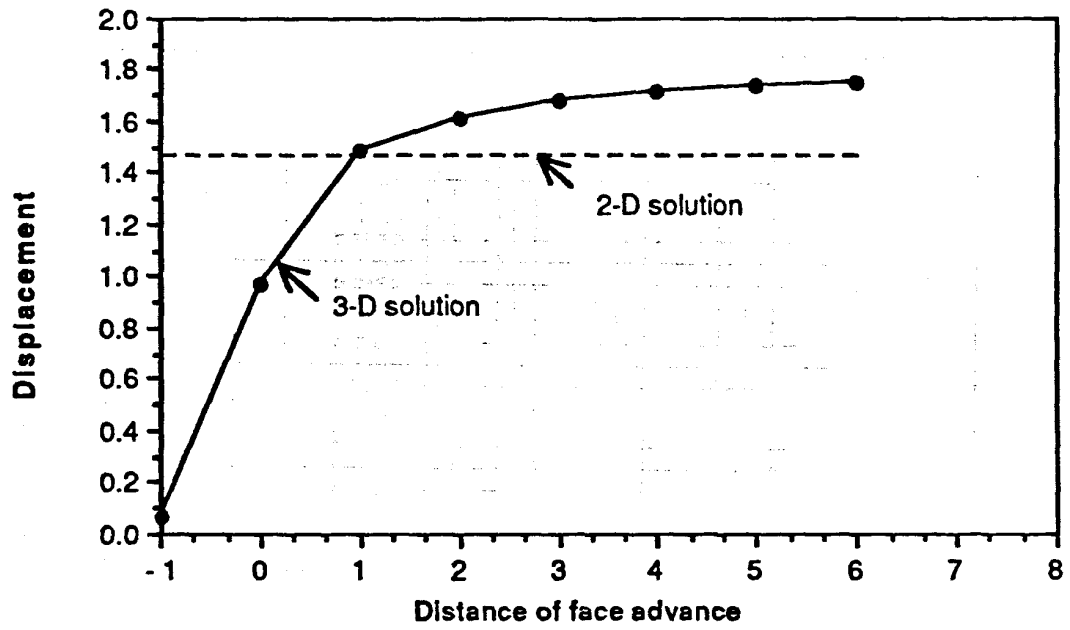


Figure 4.26 The tunnel convergence against excavation steps (simulating face advances).

the above model. Program FESTER has also proved to be a valuable tool for research in this area.

5. References

Hinton, E. and Owen, D.R.J. (1977) *Finite element programming*: Academic Press. London.

Hoek, E. and Brown, E. T. (1988) The Hoek-Brown failure criterion-a 1988 update. In *Proc. 18th Canadian Rock Mechanics Symp.*, Toronto, Canada.

Naylor, D.J. (1977) FINEPAK (Mark 2): User instructions and explanatory notes. Univ. College Swansea, Dept. Civil Ebgng. Report CR/85/76.

Pan, X.D. (1988) Numerical modelling of rock movements around mine openings. PhD thesis, University of London (Imperial College).

Pan, X.D. and Hudson, J.A. (1988) Plane strain analysis in modelling Of 3-D tunnel excavations, *Int. J. Rock Mech. & Min. Sci. & Geomech. Abstr.*, Vol. 25, No. 5, pp 331-337.

Pan, X.D., Hudson, J.A. and Cassie, J. (1989) Large deformation of weak rocks at depth. In *Rock at Great Depth*, Maury & Fourmaintraux eds., Balkema, Rotterdam, pp 613-620.

Reed, M.B. (1986a) Numerical solutions for the axisymmetric tunnel problem using the Hoek-Brown criterion. In *Numerical Models in Geomechanics*, G.N. Pande and W.F. Van Impe eds., M. Jackson, Redruth, pp 369-374.

Reed, M.B. (1986b) Stresses and displacements around a cylindrical cavity in soft rock. *I. M. A. J. Appl. Math.* 36, pp 223-245.

Reed, M.B. (1988a) A elasto-viscoplastic model for soft rock. *Ing. Compt.* 5, pp 65-70.

Reed, M.B. (1988b) Nonassociated flow rules in computational plasticity. In *Num. Meth. in Geomech.*, Insbruck, G. Swoboda ed. AA. Balkema, Rotterdam, pp 481-488.

Reed, M.B. and Lavender, D.A. (1989) FESTER - An elasto-viscoplastic finite element program for geotechnical applications. Technical report and user manual, Dept Math, and Stats., Brunel University.

Zienkiewicz, O.C. and Pande, G.N. (1977) Time-dependent multilaminade model of rocks - a numerical study of deformation and failure of rock masses. *Int. J. Num. Anal. Meth. Geomech.*, Vol. 1, pp 219-248.

**NOT TO BE
REMOVED**
FROM THE LIBRARY

XB 2321427 9

